10-30-2020

Comprehensive Approach to Characterizing Tool Steel Damage Mechanisms

Alexandra Rose
University of Windsor

Comprehensive Approach to Characterizing Tool Steel Damage Mechanisms

By:

Alexandra Rose

A Thesis
Submitted to the Faculty of Graduate Studies
through the Department of Mechanical, Automotive & Materials Engineering
in Partial Fulfillment of the Requirements for
the Degree of Master of Applied Science at the
University of Windsor

Windsor, Ontario, Canada

2020

Comprehensive Approach to Characterizing Tool Die Damage Mechanisms

by

Alexandra Rose

APPROVED BY:

V. Stoilov
Department of Mechanical, Automotive & Materials Engineering

D. Northwood
Department of Mechanical, Automotive & Materials Engineering

D. Green, Co-Advisor
Department of Mechanical, Automotive & Materials Engineering

A. Alpas, Co-Advisor
Department of Mechanical, Automotive & Materials Engineering

June 1, 2020

Declaration of Originality

I certify that, to the best of my knowledge, my thesis does not infringe upon anyone's copyright nor violate any proprietary rights and that any ideas, techniques, quotations, or any other material from the work of other people included in my thesis, published or otherwise, are fully acknowledged in accordance with the standard referencing practices. Furthermore, to the extent that I have included copyrighted material that surpasses the bounds of fair dealing within the meaning of the Canada Copyright Act, I certify that I have obtained a written permission from the copyright owner(s) to include such material(s) in my thesis and have included copies of such copyright clearances to my appendix.

I declare that this is a true copy of my thesis, including any final revisions, as approved by my thesis committee and the Graduate Studies office, and that this thesis has not been submitted for a higher degree to any other University or Institution.

Abstract

Tool steels with increased wear-resistance are being developed for use in trimming operations to improve tool life and final part quality. This study investigates Uddeholm Carmo and Caldie, tool steels exhibiting microstructures with small, evenly distributed carbides. The microstructure and mechanical properties of these steels are compared to D2, a conventional tool steel with much larger bands of carbides. Tests were conducted using miniature tensile, shear compression, and compression specimens. Digital image correlation (DIC) strain measurements were used to develop flow curves. Material characterization and analysis of fracture surfaces were carried out using SEM. Trimming trials were conducted with D2, Carmo, and TiCN PVD coated Caldie. The profiles of the trim edges were captured using optical profilometry. Carmo and Caldie showed increased fracture stresses and strains compared to the conventional D2. In Caldie, there was as much as 169% and 281% increase in stress and strain respectively in tension compared to D2. This resulted in a reduction in material loss on the trim edge. The fracture surfaces revealed a primarily brittle fracture in D2, with the cleavage fracture of the large primary carbides being the dominant mode of fracture in all of the tests conducted. Carmo and Caldie fractured with dimples composed of local quasi-cleavage fracture as its dominant fracture mode. It can be concluded that the smaller, more evenly dispersed carbides in Carmo and Caldie improved their mechanical properties and had a positive effect on the fracture toughness and wear resistance.

Acknowledgements

I would first like to give my sincerest thanks to Dr. Daniel Green and Dr. Ahmet Alpas for their incredible guidance. Their continual patience and support gave me the best possible atmosphere I could hope for. I truly appreciate all of the opportunity I've been given to learn. Thank you for pushing me to always bring my best work to the table, and for your guidance and expertise through the last three years.

I would also like to thank the rest of my committee: Dr. Northwood and Dr. Stoilov for their guidance and support and for bringing so much wonderful discussion to my work. I would like to take this opportunity to thank the technical staff and secretaries at the University of Windsor, without whom I wouldn't have been able to complete this work.

Thank you so much to my wonderful research group. In particular, Iman, Yang, and Zeyuan, I'm so grateful for the high bar you have all set and the conversations I've been able to take part in. Thank you to Liza Dicecco, who has kept me sane since my first week of university. To Spencer Paddon who emotionally supported me through my degree. Special thanks go to my best friend of too many years to count, Courtney Zamparo, who has been like a sister and has always been there for me.

Finally, to my parents, who have always supported me and cheered me on. Thank you for your constant love and sacrifices.

Contents

List of Abbreviations

AHSS	Advanced High Strength Steel
DP	Dual Phase Steel
DIC	Digital Image Correlation
OM	Optical Microscopy
SEM	Scanning Electron Microscope
BSE	Back-Scattered Electron
E	Young's Modulus
EAF	Electric Arc Furnace
ESR	Electro-slag remelting
TRIP	Transformation Induced Plasticity Steel
PVD	Physical Vapor Deposition
CVD	Chemical Vapor Deposition

List of Figures

Chapter 1

Introduction

Improvements to high strength steels in the automotive industry result in improvements to impact resistance and passenger safety. The corporate average fuel economy (CAFE) standards prompted the development of advanced high strength steels (AHSS). The CAFE standards were established by the National Highway Traffic Safety Administration (NHTSA) to counteract the effects of the 1973 oil crisis. The high fuel prices of the 1970s incentivized automotive manufacturers to increase engine efficiency and reduce weight in their vehicles [1]. Stronger steel grades, such as AHSS, allow for sheet thickness reduction while maintaining the same or greater impact resistance. However, the development of these materials has introduced challenges to the manufacturing process.

The higher strengths exhibited by AHSS when compared to traditional mild steels lead to higher contact pressures in trimming operations. An increase in contact pressure generally increases the severity of the wear [2]. Trimming operations, in particular, are subject to many increases in cost with increased tool wear. Burr heights are shown to increase with tool wear [3], which adds costs to the parts manufactured because of a need for an additional deburring process. Tool wear can also affect the edge stretchability of the sheared part, as shown in Figure 1.1. As the tool wear increases, the edge formability decreases as depicted in Figure 1.1b, where the strain at fracture decreased with increasing die usage.

Figure 1.1a shows that edge stretchability decreases due to the change in failure mode from ductile necking to more brittle fracture with an increasing number of trimming cycles [4]. This phenomenon leads to more splits and tears in the subsequent forming processes.

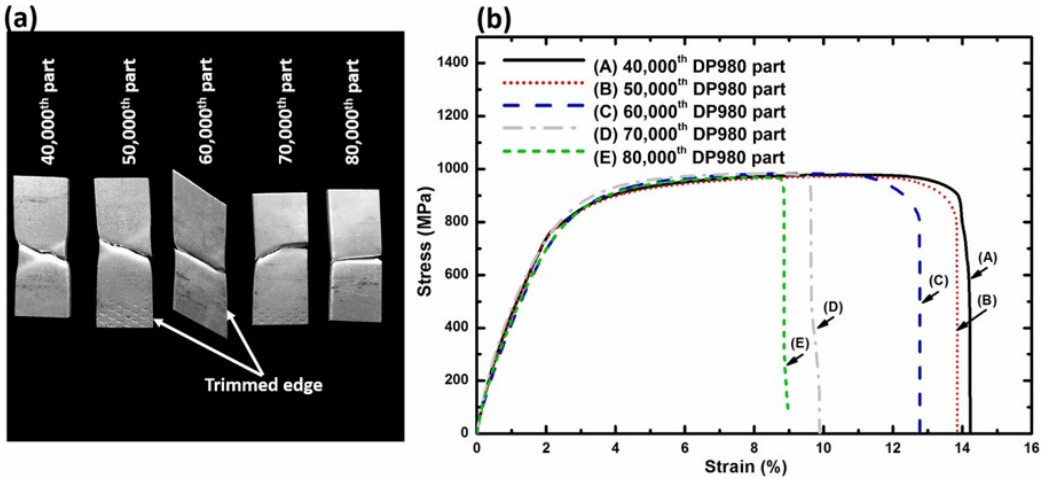

Figure 1.1: (a) Failure modes and (b) tensile stress-strain curves of trimmed DP980 sheets [4].

The solution implemented in industry is to develop new, more wear-resistant, tool steels. Uddeholm can be credited for their development of Carmo and Caldie, tool steels that provide improved wear and chipping resistance over traditional options such as D2 steel in industrial trimming operations. These three cold work tool steels are of particular interest in this study. D2 steel is composed of approximately 12% chromium and 1.5% carbon. Carmo and Caldie were developed to reduce this to approximately 4.5-5% chromium and 0.6-0.7% carbon and use multiple tempering processes. The differences in composition, processing and heat treatment between these tool steels combine to produce different mechanical and wear properties. Figure 1.2 shows the hardened microstructures of Sverker 21, Uddeholm's D2, and Caldie. It will be shown that the difference in microstructures has a significant influence on the macro-scale properties.

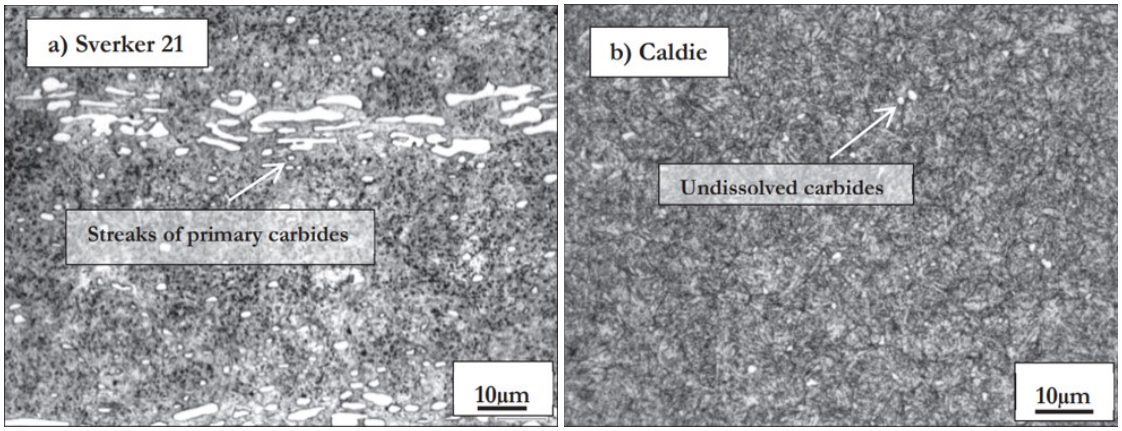

Figure 1.2: Optical micrographs of a) Sverver21 (1.5% C and 12% Cr) and b) Caldie (0.6-0.7% C and 4.5-5% Cr) [5].

1.1 Research Questions

There exists a gap in the knowledge regarding the characterization of new tool steels, and the methods available to quantify the improvements made and what changes can be made to further improve the materials. The following research questions were developed with this in mind:

1. How might we characterize tool steels in a way that is meaningful and objective?
2. How do the differences in processing and microstructure between D2, Carmo, and Caldie, affect their mechanical properties?
3. How can the resulting trim die wear be objectively quantified for validation and comparison to the mechanical properties?

1.2 Material Science Tetrahedron

One of the best ways of studying materials is described by the material science tetrahedron. It can be broken down into four fields of study, represented as points on the tetrahedron, as shown in Figure 1.3. These four aspects are related to each other and each one influences the development and selection of materials. This tetrahedron is a powerful tool

that correlated the various elements of materials science together. Through understanding each aspect of material science and how they relate to each other, a roadmap can be made to thoroughly characterize a particular material.

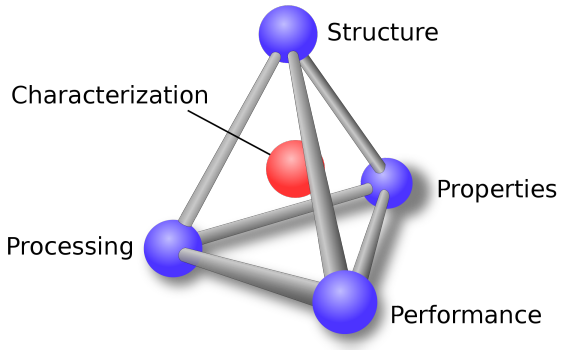

Figure 1.3: Traditional material science tetrahedron [6].

The materials and heat treatment were predefined for this study, which relate directly to the structure and processing. The material science tetrahedron is used to determine the remaining critical areas of research: the properties and performance. This study will identify the properties and performance of D2 steel, Carmo, and Caldie and draw conclusions on the links between the structure, properties, processing, and performance. This will result in a comprehensive characterization of these tool steels.

Chapter 2

Tool Steels

Tool steels are typically hard, tough steels with some level of wear resistance. They are used in forming, cutting, and trimming operations. There are several types of tool steel available, depending on cost and application. The AISI classification of tool steels is given in Table 2.1 [7]. As shown, tool steels can be grouped by a diverse number of characteristics, either through mechanical properties, heat treatment, or composition. The limiting factor for this study is the application. Cold-work tool steels are beneficial in trimming operations when compared to tool steels such as one within the high-speed steel category. Higher alloy contents are used to establish high-temperature stability and wear resistance in high-speed tool steels which are not required in room-temperature trimming operations and may drive up costs.

AISI Symbol	**Tool Steel**
M	Molybdenum High-Speed Steels
T	Tungsten High-Speed Steels
H	Hot-Work Steels
A	Air-Hardening, Cold-Work Steels
D	High-Carbon, High-Chromium, Cold-Work Steels
O	Oil-Hardening, Cold-Work Steels
S	Shock-Resisting Steels
P	Low-Carbon Mold Steels
W	Water-Hardening Steels

Table 2.1: AISI Standard designation of tool steels [7]

2.1 Production of Tool Steels

Conventional electric arc furnace (EAF) casting and powder metallurgy are the two primary methods of creating tool steels. In conventional EAF casting, scrap steel is melted in an electric arc furnace. The steel is then refined primarily in a ladle furnace, which is used for deoxidation, decarburization, adjustment of chemical composition and possibly inclusion shape control to improve material properties. This is done to produce an overall clean steel. This is followed by further refinement in a vacuum ladle degassing unit, where the molten steel is stirred through the use of induction coils and argon is bubbled through the molten steel in a vacuum tank to deoxidize and desulfurize the steel [8, 9]. The steel is then solidified; typically in an up-hill casting unit [5]. This method of production is cheap, produces a consistent product, and is very widespread.

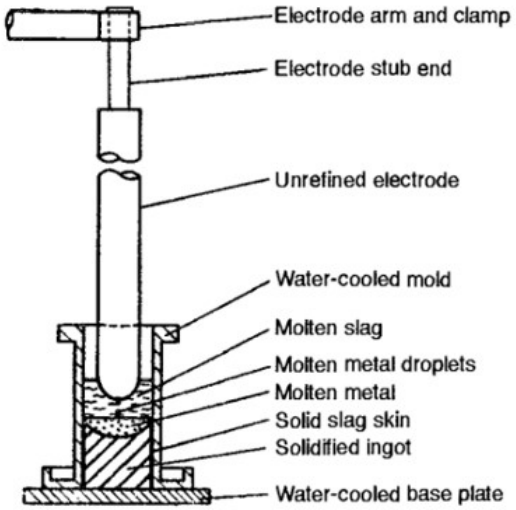

Figure 2.1: Depiction of ESR process [8].

Electro-slag remelting (ESR) is an additional processing step used to improve the overall quality of the steel. A conventional ingot is used as an electrode; it is then melted in a molten slag. The ingot material settles at the bottom due to its higher density when compared to the slag, and solidifies. This allows for thin layers of solidified material to accumulate into a final product. The slag can also be made to desulfurize and dephosphorize as well. Figure 2.1 depicts this process and shows several of the elements discussed. ESR is shown to produce final ingots with smaller carbides and grain sizes, higher chemical uniformity, less carbide banding, better tensile ductility, and improved fatigue properties [8, 9].

After the final ingot of steel is produced, it is typically soaked in a pit to homogenize the microstructure. The areas of the cast ingot which contact the casting mould will generally cool more quickly than the center [5, 9].

2.2 Heat Treatment

Tool steels that require an additional heat treatment process are sold in the annealed state. In this way, they can be machined before hardening. After the steel is machined, it is pre-heated to reduce the amount of distortion brought about by austenitization. It is then heated up to a temperature that brings the steel to a structure composed of austenite and undissolved carbides. If the temperature is too high, it will result in too much retained austenite in the quenched steel. The quenching medium of the steels has a large influence on the final constituents found in the steel. A sufficiently fast cooling rate results in a steel composed of martensite and carbides. Slower quenches can result in the formation of ferrite, pearlite, and bainite [11].

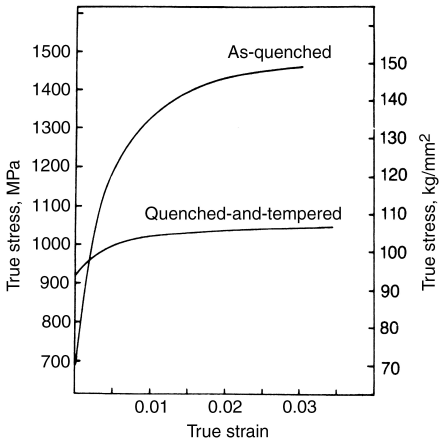

Figure 2.2: Difference in mechanical behaviour of Fe-0.2C as-quenched and tempered lath martensite [10].

As-quenched martensite is inherently brittle and must be tempered to regain some ductility. This process also decreases the strength and hardness of the steel. The effect this has on the mechanical properties of the steel can be seen in Figure 2.2. Hardness can be returned through the inclusion of alloying elements. Careful alloying can result in the formation of nano-sized MC and M_2C carbides in this stage, causing ”secondary hardening” [5, 10].

Upon cooling from the temper, retained austenite in the structure can transform into martensite. The newly transformed martensite is not ideal, as it is not tempered and thus very brittle; additionally, a single temper treatment may be inadequate in transforming

the remaining retained austenite. Multiple tempering treatments may be applied to fully transform the remaining austenite and temper the newly formed martensite [5].

2.3 Alloying Elements

Beyond the processing and heat treatment, the microstructure and properties of the tool steels are influenced by the alloying elements. Chromium above 12 wt% acts to protect the steel from corrosion; even in lower quantities it stabilizes martensite, improves tensile strength and hardness, and initiates the formation of carbides. In particular, M_7C_3 and $M_{23}C_6$ carbides are found in chromium-rich steels. Chromium and molybdenum increase the hardenability of tool steel. M_6C and M_2C are both molybdenum-rich carbides that form in tool steels. It has also been shown that molybdenum plays a role in the distribution of MC carbides in high-speed tool steels [12]. Another alloying element that promotes carbide formation is vanadium. Vanadium, like chromium, also increases the tensile strength; it also improves impact, fatigue and wear resistance in steels. Vanadium is also a key component of very small MC carbides that aid in secondary hardening. Silicon is responsible for improving tensile strength, hardness, and yield point, though negatively impacts elongation. Manganese improves impact strength and plasticity [9, 13].

2.4 Microstructure

Cold work steels (groups A, D, and O) are of interest due to their high hardness and wear-resistance in cold work applications. The microstructures are relatively similar for each tool steel, barring a difference in volume fraction of martensite, retained austenite, and carbide size and distribution.

Martensite forms as a body-centred tetragonal (BCT) structure in ferrous materials through a diffusionless transformation from face-centred cubic (FCC) austenite through rapid quenching. This inherently hard and brittle phase makes up the matrix of cold-work tool steels. It is typically tempered to return some of the ductility and toughness required in operations such as trimming, where the formation of cracks/chips is a concern. Retained

austenite is what is leftover in the transformation, as not all of the austenite is transformed. It is capable of being transformed into martensite through deformation as in the case of transformation induced plasticity (TRIP) steels. There is typically an order of magnitude of $<2\%$ to 10% retained austenite depending on the tool steel and heat treatment in the tool steels being studied. Carbides are distributed throughout the tempered martensite matrix. These carbides are affected by the heat treatment and composition of the steel. They can generally be divided into 'primary carbides' and 'secondary carbides,' where carbides over 5-10 μm are considered primary carbides, and those below that threshold are considered secondary carbides [14].

As the critical microstructural feature in tool steels, carbides play a significant role in the behaviour of the bulk material. It has been shown that the alloying elements which make up second phase particles affect the bulk material properties, as their ability to bond with the matrix will determine the strengthening effect of the particles. The bond between the particles and the matrix must overcome the shear stress across the interface. This strengthening effect is then dependent not only on the bond but also on the mean free path of the particles, as defined by Fullman et al. [15]. The yield strength decreases as the mean free path increases until a critical mean free path is reached, at which point the particles no longer have a strengthening effect. This limit to the strengthening effect is also dependent on particle size. The same study showed that while the particle distribution, size, and composition affect the yield strength of the material, embrittlement is independent of these factors and depends only on volume fraction. The particles act as a strain concentrator, similar to a notch in a test specimen, which causes the material to locally fracture prematurely [16]. This has been confirmed in more recent studies, as it has been shown that the fracture toughness decreases with an increased fraction of total carbides [17]. These are essential considerations when looking to improve materials and material microstructure for use in trimming operations since fracture toughness and strength play a significant role in the tool's resistance to chipping.

2.5 Effects of Microstructure on Wear Resistance

In past work looking to define the wear shown in tool steels, three damage mechanisms were identified; chipping, galling, and abrasive wear [14, 18, 19, 20]. Galling is defined as an adhesive wear where the softer material adheres to the harder die surface. Abrasive wear is characterized by material removal or plastic deformation in scratches or score marks. These are not as catastrophic or as severe as chipping, which occurs when large pieces of the harder tool steel are suddenly removed.

2.5.1 Balance of Hardness and Toughness

Archard and Hirst were the first to develop a relationship between wear rate, applied load and hardness [21]. This relationship holds true in die materials. A correlation exists between the hardness of a die material and its ability to resist wear [22]. Decreasing the volume fraction of retained austenite can be used to increase the hardness, and thus wear resistance of the steel. This is typically done through cryogenic treatment or through high temperature tempering where additional martensite is transformed in each subsequent tempering cycle [5, 23, 24].

The presence of retained austenite increases the fracture toughness in steels, as the crack induced transformation to martensite causes compression and blunting of the crack tip and reduces what energy is available for further crack propagation [25]. An increase in fracture toughness would work to resist chipping, as the crack propagation required for chipping to occur would require more energy.

2.5.2 Influence of Carbides on Wear Resistance

One of the important characteristics of tool steel is the small, more evenly distributed carbides in the material [23]. Ko et al. [14] compared three types of D2 steels, with varying hardnesses and carbide types, using a pin-on-flat tribometer under dry condition. Tests were conducted using a pin with a tip radius of 5mm and a normal load of 200N. An increase in hardness resulted in better wear resistance. Two steels were tested with similar hardnesses. In this case, a large factor was the type, size and distribution of carbides.

Optical micrographs of the three steels used are shown in Figure 2.3. The material shown in Figure 2.3c (Tool B) with the smaller, evenly distributed, secondary carbides showed an increase in wear resistance of 16.7% over the conventional D2 tool steel, which had larger, rouch carbides, greater than 5μm. The material shown in Figure 2.3b (Tool A) had a smaller volume percentage of carbides than the D2 tool steel. The carbides in Tool A were also larger and less evenly distributed than Tool B and showed an increase in wear resistance of 4.56% over the standard D2 steel.

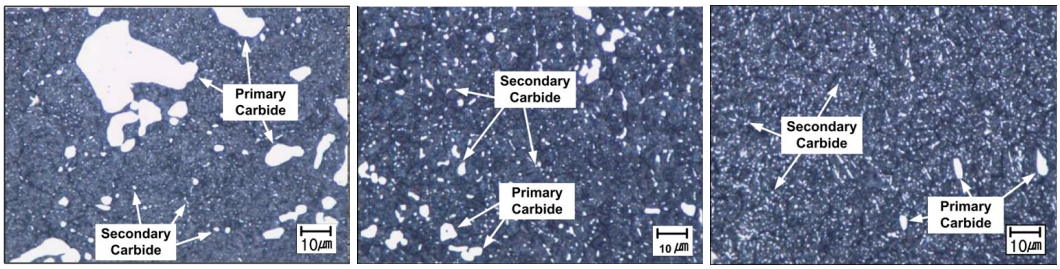

(a) D2 (b) Tool A (c) Tool B

Figure 2.3: Optical microscopy images depicting difference in carbide distribution [14].

One of the important characteristics of tool steel after cryogenic treatment is the fine, evenly distributed carbides in the material when the treatment is implemented between quenching and tempering of the material [23]. Das et al. [24] found a 5% increase in hardness after cryogenic treatment, which was not significantly affected by the length of holding time at cryogenic temperature. There is a slight increase in wear resistance for the material cryogenically treated for 36 hours (QCT36) when compared to the material cryogenically treated for 84 hours (QCT84). This can be seen in Figure 2.4 . The difference was explained by carbide formation. A large difference can be seen between the carbides present in the conventionally quenched and tempered (QT) samples when compared to the QCT

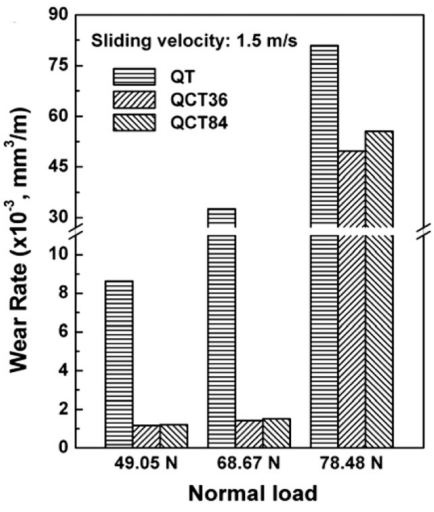

Figure 2.4: Wear rate with respect to normal load [24].

samples. The number of large secondary carbides (LSC), which are approximately 0.5-2.0μm in diameter, are more numerous in the SEM micrograph of the QT sample than the QCT samples, shown in Figure 2.5. The important characteristic which distinguishes the QCT36 and QCT84 samples are the finer and more evenly distributed small secondary carbides (SSC) in the QCT36, which are approximately 0.1-0.5μm in diameter. This is expected to be the reason for the increase in wear resistance of the QCT36 samples over the QCT84 samples.

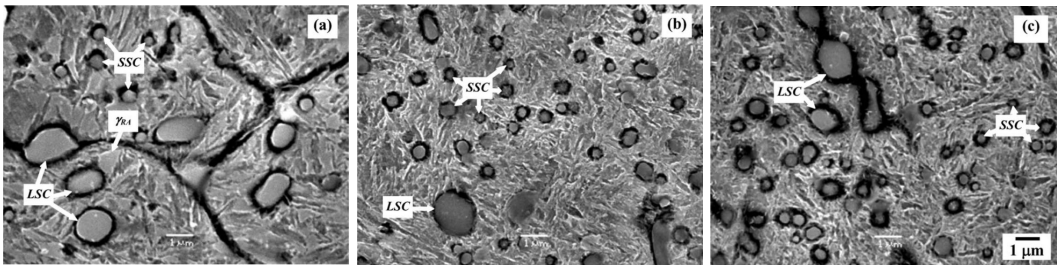

Figure 2.5: High magnification SEM micrograph of (a) QT (b) QCT36 and (c) QCT84 samples [24].

2.6 Fracture Behaviour of Tool Steel

As tool steels tend to be brittle, it is important to understand their fracture behaviour. The microstructure has a large effect on the dominant mechanisms responsible for fracture. There are three modes of fracture that can occur; ductile, cleavage, and quasi-cleavage. Ductile fracture occurs when the material is able to plastically deform and thus, deforms around impurities, voids, or harder second phase particles in the material and creates what is called a ”cup or cone” fracture. Cleavage fracture occurs in brittle materials and is defined by a series of low index planes which follow certain crystal orientations, which have been ”cleaved” by the propagation of microcracks and look like plateaus on the surface. Quasi-cleavage fracture occurs when the material forms micro-cracks which are independent of crystal orientation, and form small ridges when the material fractures. This type of fracture appears cleavage-like; however, it does not occur along the cleavage plane. A schematic showing quasi-cleavage fracture can be seen in Figure 2.6 [26].

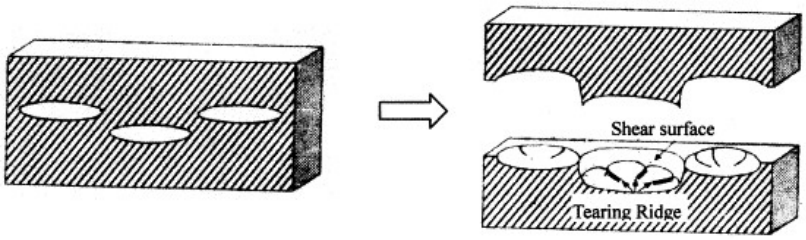

Figure 2.6: Schematic depicting quasi-cleavage fracture [26]

Further images showing quasi-cleavage fracture in tool steel are given in Figure 2.7. Figures 2.7a and 2.7b show a dimpled H11 notched tensile surface. At the higher magnification it can be seen that these dimples contain local quasi-cleavage fracture. Figure 2.7c shows quasi-cleavage fracture that was revealed in a high speed tool steel. The quasi-cleavage fracture was associated with a tempered martensite matrix composed of plate martensite.

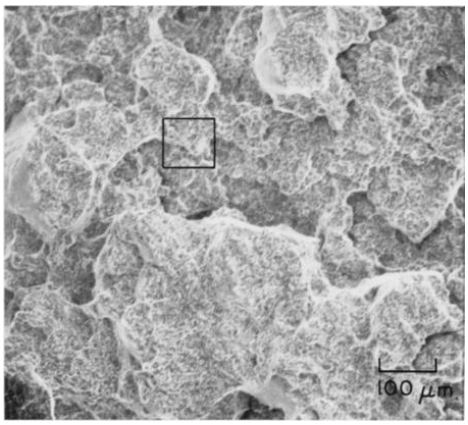

(a) H11 SEM X100 [27]

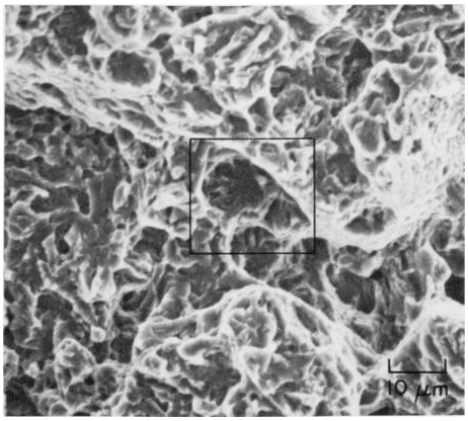

(b) H11 SEM X1000 [27]

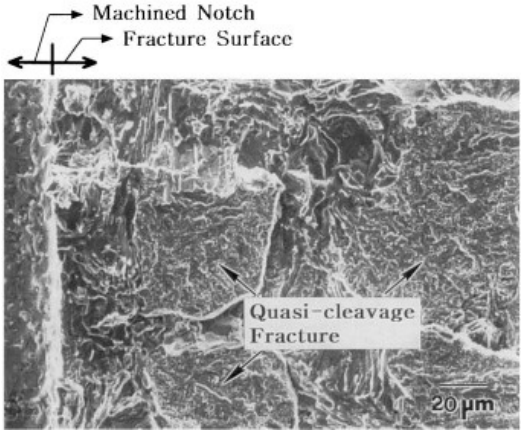

(c) HSS SEM Fracture Surface [17]

Figure 2.7: Examples of Quasi-cleavage fracture in tool steel

2.6.1 Effect of Microstructure on Tool Steel Fracture Behaviour

The size and distribution of carbides have been shown to affect the wear behaviour of tool steels. This extends to the mechanical behaviour as well. Fracture initiation has been shown to occur at primary carbides which tend to be distributed along cell boundaries. Brittle fracture of carbides does nothing to slow the propagation of cracks. Small carbides distributed within the tempered martensite cells is ideal, as the relatively ductile fracture of the tempered martensite delays fracture. This allows the carbides to contribute to higher hardness and better wear results without contributing to the fracture of the bulk material [17, 28].

The contribution that large primary carbides have on crack initiation can be seen in Figure 2.8. Figure 2.8a shows the cracking which occurred in the carbide located in close proximity to the surface, and Figure 2.8b shows fracture in a similar part. In both cases, ductile failure can be seen in the matrix, with crack initiation appearing to be due to brittle, ”massive” carbides fractured near the part surface[29].

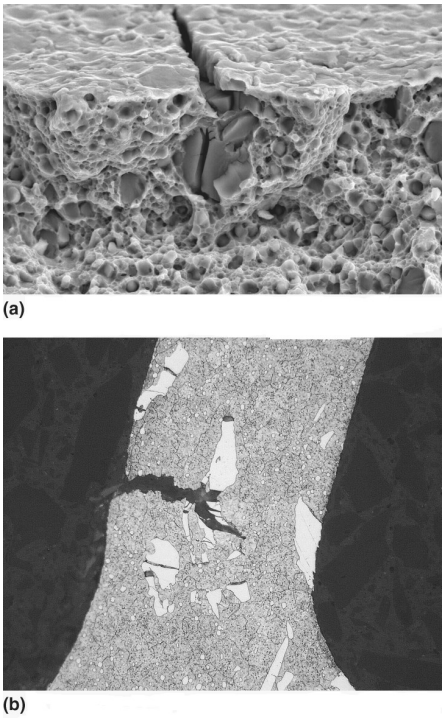

Figure 2.8: Fracture in D2 [29].

In a study by Hwang et al. [12], the effect of alloying elements in HSS were considered in relation to the types of carbides formed, and where they were likely to form. Generally, the alloying elements had benefits to the general material properties or the distribution of certain carbides. An excess of any one alloying element results in the formation of many carbides along the cell boundaries. For example, chromium acts to precipitate fine carbides, and has been shown to have a secondary hardening effect in the tempering of steel at high concentrations. However, it was found that many M_7C_3 carbides form in the cell boundaries when there is more than 7% Cr [12][30]. This study also revealed effects of the

carbon content on the type of martensite, both from prior literature [30], and from visual appearance of the as-cast HSS. It was shown that lath martensite forms in alloys with a matrix containing less than 0.4%C, and plate martensite forms in alloys with over 0.4%C. The cracking of the plate martensite was identified as the cause of quasi-cleavage fracture, shown in Figure 2.7c, as the dominant fracture mode in the steel mostly containing the relatively ductile lath martensite showed either a mixed fracture mode, similar to that shown in Figure 2.8 or predominantly cleavage fracture [17, 12].

2.7 Effect of Coatings on Wear Behaviour

Another method used to reduce tool wear is to coat the die. This allows for a change in the wear mechanisms due to the presence ofa new interfacing material. As with the substrate material, there is a need to understand the microstructure of the coatings used. The microstructures of physical vapor deposition (PVD) and chemical vapor deposition (CVD) have been characterised by Fortuna et al. [31]. PVD coatings were determined to have high local residual stress levels, with non-equiaxed grain structures, with grain sizes of 0.1-0.2μm. A schematic of this grain structure is shown in Figure 2.9a. This is in contrast to CVD coatings which have a low residual stress and an equiaxed micro-crystalline structure, with grain sizes of 0.4-0.6μm as depicted in Figure 2.9b.

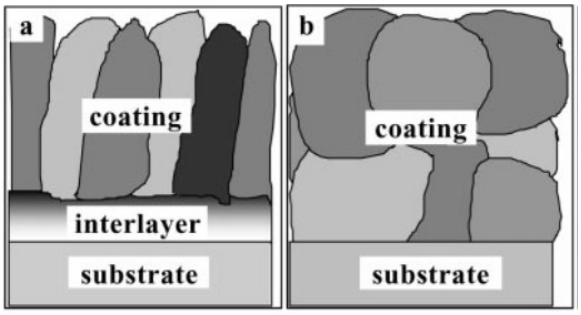

Figure 2.9: Schematic of grain microstructures of (a) PVD, and (b) CVD coatings [31].

PVD coatings make use of sputtering or evaporation to deposit a thin layer of material onto the substrate. In sputtering, the coating material and substrate are placed in a vacuum chamber. The coating is given a negative charge. An inert gas is introduced and the coating

is discharged onto the substrate. Evaporation deposition also occurs in a vacuum chamber, and the coating is heated to evaporation. The coating then condenses onto the substrate [32]. CVD coatings begin as gaseous chemical reactants which are thermally activated on the substrate and form a solid deposit [32].

Thermal diffusion (TD) coating is a method which allows for high adhesion with minimal equipment cost. The substrate and coating are heat treated together to allow the coating material to adhere to the substrate material [33]. This method could require further processing of the die, as the material must be quenched and tempered after coating [34]. The effects of coatings and substrate material were investigated using a cylindrical test specimen being dragged across a DP 1000 sheet [34]. This study compared CVD, PVD, and TD coatings on the same substrate, and then TD coatings on four different substrates. It was found that the leading edge of the cylindrical specimen showed scoring, suggesting a chipping type wear, and the trailing edge showed thin cracks perpendicular to the sliding direction. These cracks were representative of an adhesive-type of wear, as the coating layer broke and peeled away from the substrate. A picture of the typical test specimen after testing is shown in Figure 2.10a, alongside images of the cross-section before and after testing, showing the removal of the coating in Figure 2.10b and c. There was also evidence of fatigue cracking in the trailing edge due to compressive and shear forces. Energy dispersive X-ray spectroscopy (EDX) was used to characterise the worn surface. It showed that the worn surfaces were completely devoid of coating. The trailing edge was also shown to have evidence of sheet material transfer to the voids in the cracked coating. Overall, the TD coating showed the highest wear resistance, followed by the TiCN PVD layered coating, then the multilayered CVD coating.

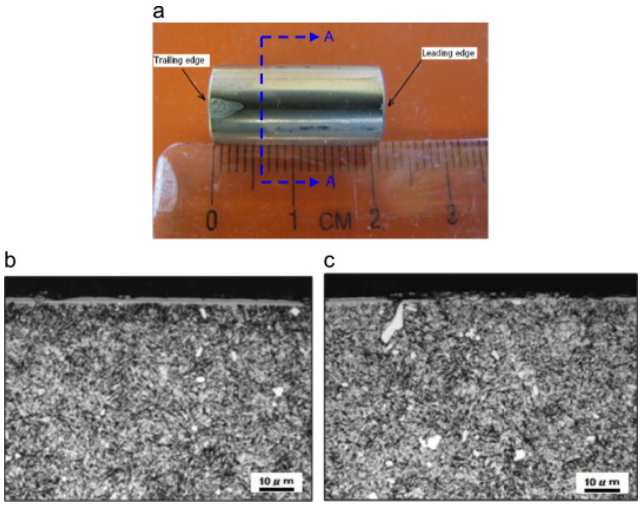

Figure 2.10: (a) Image of a worn specimen with the leading edge to the right, and a cross section of a TiCN PVD coated specimen (a) before and (b) after testing [34].

The different coating and substrate pairs yielded different wear rates. It was determined that the substrate hardness influenced the effectiveness of the coating. A harder substrate caused the coating to have better adherence to the substrate, which allowed for an increased wear resistance [34].

In another study by Cora et al. [35], a different testing method and counterface were used to test the same coatings. In this study, a CNC pushes a bullet shaped sample across a DP600 steel sheet. The purpose is to better represent a forming process, as the bullet shape can achieve higher contact stresses than a pin sample and does not interact with the same counterface repeatedly [19]. Instead it is constantly in contact with new sheet material, much like a forming or trimming die would be. In this study [35], wear tracks were much more visible in the PVD coated sample, and the authors observed adhesion wear. Though there is a correlation between substrate hardness and wear resistance in both papers, this is not the case for the coating hardness. A higher coating hardness did not ensure a lower wear rate. It is speculated that this is due to a brittleness effect, where the coating was more likely to break and separate from the substrate at higher hardnesses [35].

2.8 Wear of Tool Steels in the Literature

2.8.1 Lab Scale Tribometers

The ball-on-disk or pin-on-disk tribometers do not give a true representation of the wear seen in forming and cutting applications. Tests such as those conducted by Cora et al. [35][19] represent advances in the appropriate tests that can be applied to simplify the forming or cutting processes. This is an issue seen in many publications, as the tool will not be in repeated contact with the same area. It is not affected by previous changes in profile or work hardening of the sheet material as it would be in a typical pin-on-disk test.

D2, Carmo, Caldie, and several other tool steels were compared when sliding against DP600. Of these three tool steels, Carmo exhibited the lowest wear rate. The authors suggested that due to the low hardness of the Caldie provided for the study, the Caldie samples did not perform as well as expected. The Carmo and Caldie exhibited primarily abrasive wear leading to material loss. The D2 steel sample was the only one to exhibit galling.

2.8.2 Lab Scale Trimming Trials

Past studies have investigated the effect of trimming on tool steels in lab scale trimming trials. This is the best way to evaluate and compare tool steels, as the number of assumptions is reduced and the results can be most easily transferred to industrial applications. Unfortunately these trials often cost more and require more forethought than traditional characterisation methods such as tensile tests and pin-on-disk tests.

Trials performed using a Ford-commissioned commercial scale trimming press considered the interactions between D2 and DP980 in trimming operations. Wear on the die edge was observed using optical profilometry after intervals of 20,000 trimming cycles up to 80,000 trimming cycles. As a way of adequately defining the wear using optical profilometry, two faces are identified on the trimming die. These are labelled as the XY (impact) and YZ (sliding) planes, as shown in Figure 2.11.

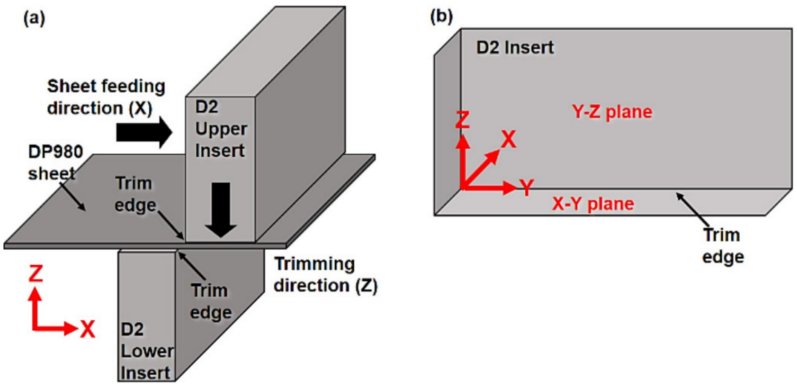

Figure 2.11: Schematic representation of the coordinate system assigned to the faces of the trimming die (a) in terms of the trimming direction and location of the sheet material and (b) labelled on the insert itself [18].

The wear observed took the form of abrasive wear, plastic deformation, and chipping. The primary mechanism in this case appeared to be chipping. Images of the worn edge can be seen in Figure 2.12, where the dark blue areas represent missing material. It was observed that there is a difference in wear between the upper and lower dies. The lower die appears to exhibit higher chipping rates when compared to the upper die. Chipping appeared sooner (at 20,000 cycles in the upper die compared to 80,000 cycles in the lower die) and in higher volume (45% of the edge was chipped in the lower die when compared to 15% in the upper die after 230,000 cycles) in the lower die [18]. Additionally, when surface roughness measurements were taken, the sliding (YZ) plane exhibited a higher surface roughness in general when compared to the impact (XY) plane.

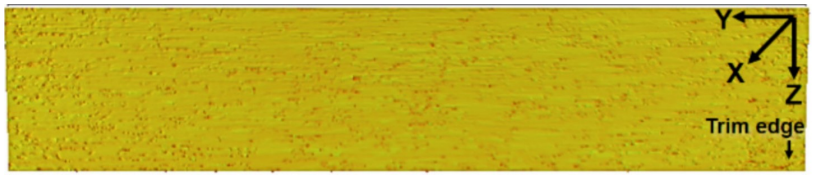

(a) Insert surface profile before trimming.

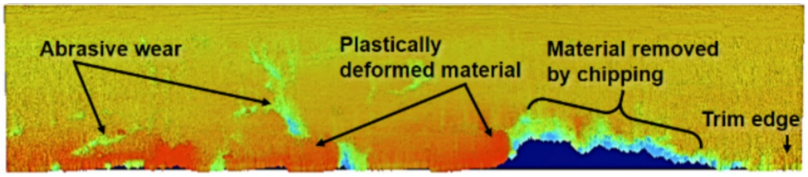

(b) Insert surface profile after 20,000 trimming cycles.

Figure 2.12: Optical profilometry images of the YZ trimming plane in the lower die [18].

Further testing of Carmo and Caldie was conducted using a commercial scale trimming press. The stationary lower die was composed of Caldie, while the upper die was composed of Carmo. Cui et al. [36] conducted the analysis. SEM of the trim die surface after 40,000 hits was done on both uncoated Carmo and TiCN PVD coated Caldie. Figure 2.13a depicts abrasive wear due to sliding, where the material has been plastically deformed in the direction of sliding. Figures 2.13b and c show the effect of sliding on the Caldie trim edge. They show that there is material loss in Caldie which can be attributed to the removal of the TiCN coating, and that beneath the coating, cracks perpendicular to the sliding direction have begun to form.

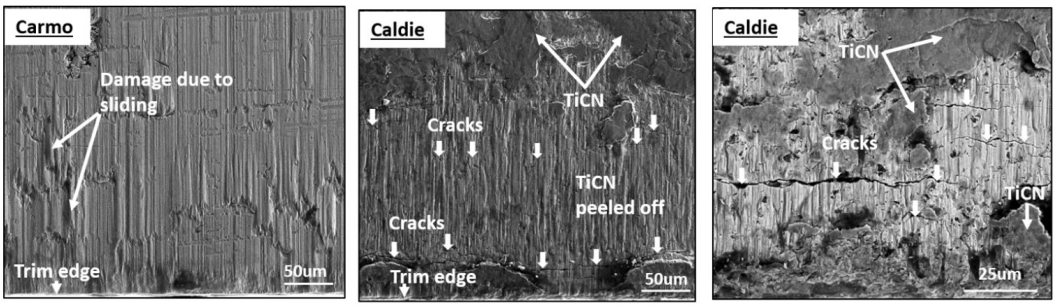

(a) SEM image of Carmo trim edge (b) SEM image of Caldie trim edge (c) Higher magnification image of Caldie trim edge

Figure 2.13: SEM near the trim die edge in YZ plane for Carmo and coated Caldie [36]

Combined cutting/forming trials in a lab scale press have been used to compare cold work steels and their interaction with an electrogalvanized CP1000 sheet material [20]. Wear on the die edge was characterized using optical light gap measurements, and external tactile measurements. These were supported by OM and SEM observations. Overall, this study used several methods to measure the wear at the trim edge locally and globally. This study considered tool pairs consisting of several Uddeholm based tool steels, Sverker21, also known as D2, Sleipner, Carmo, and Caldie. The D2 was studied in the uncoated condition as well as nitrided with a TiAlN coating. In this study, the two planes which meet at the trim edge were also labelled as the 'front surface' and the 'tool flank.' The front and flank surfaces can be related to the XY and YZ planes respectively [18, 36]. The difference being the added forming operation performed using the front surface.

The light gap measurements showed a dramatic increase in the wear in Carmo after only 20,000 cycles when compared to the other tool steel pairs. This was particularly apparent in the front surface, where the gap measured approximately 0.055mm, compared to an average of approximately 0.02mm in the other tool steel pairs. The Carmo tools were removed from the trial after 29,000 trimming cycles due to the high chipping rate and plastic deformation. Coated and nitrided D2 showed the best performance of the pairs on both surfaces. Caldie showed very little increase in wear on the front face, and showed similar wear to uncoated D2 steel on the flank face [20].

The external tactile measurements rely heavily on local wear behaviour and are not as likely to give the full picture. They may not be objective measurements as they highly depend on the number of measurements and the locations of the measurements. These results showed adhesion to the tool steel due to the zinc coating on the steel sheet. The measurements also showed the significant amount of plastic deformation in the Carmo before being pulled out of the study. The uncoated D2 steel showed noticeable plastic deformation and blunting of the trim edge as well, especially when compared to the coated and nitrided D2 steel which showed little change to its trim edge profile. The wear in uncoated D2 and Caldie were comparable overall, though the authors of the study suggests that the wear and chipping behaviour in the die is highly dependent on the study being performed [20].

2.9 Characterizing Tool Steels

One way of comparing and characterizing developed materials is through mechanical testing such as tensile tests. These tests are well established, repeatable, and standardized [37, 38]. Mechanical testing can serve to provide several outputs, including Young's modulus, yield stress, fracture strength, elongation, as well as details regarding fracture characteristics.

The damage accumulation of tool steels when used to trim AHSS can be predicted using numerical simulation. This would allow for more savings, as it would be possible to predict the evolution of wear, when to carry out maintenance, or pinpoint which tool steels

would be preferred before potentially costly long term trials. One of the roadblocks to the development of a predictive model for this purpose is the lack of information available on specific tool steels. Currently, data sheets only show the results obtained from compression tests, which includes Young's modulus and yield stress. The issue arises when attempting to input mechanical properties into a numerical model. Typically, this requires additional data spanning a range of stress triaxialities.

2.9.1 Stress Triaxiality

Stress triaxiality is the ratio of hydrostatic pressure to the von Mises equivalent stress, given by Eq. 2.1. It is a way of understanding multiaxial loading effects on a particular material.

$$\eta = \frac{\sigma_h}{\sigma_{eq}} = \frac{\frac{1}{3}(\sigma_1 + \sigma_2 + \sigma_3)}{\frac{1}{\sqrt{2}}\sqrt{(\sigma_1 - \sigma_2)^2 + (\sigma_2 - \sigma_3)^2 + (\sigma_3 - \sigma_1)^2}} \tag{2.1}$$

Fig 2.14 shows the comparison of several damage models to experimental data for a DP590 steel. As shown, the material exhibits a variation of fracture strain with stress triaxiality. This can be explained by the different stress states exhibited at key stress triaxialities. To the left, in the negative stress triaxiality region, the sample undergoes compression and exhibits a very high fracture strain, due to the suppression of cracks and voids which would typically lead to failure in a positive stress triaxiality region, where it would undergo tensile stresses. To this effect, it is important to include these results in the characterization of tool steels as they undergo a complex array of stress triaxialities in the course of trimming.

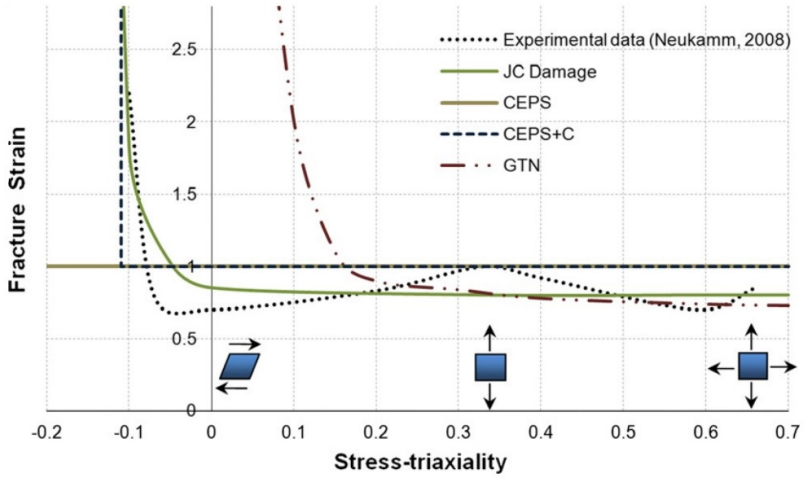

Figure 2.14: Schematic of the fracture strain with respect to the stress triaxiality for different damage criteria [39].

2.10 In Summary

As stronger sheet metals are developed, the tool steels used to form and cut these steels must continue to improve. Processes such as electro-slag remelting (ESR) can produce steels with improved microstructure over those that do not undergo this process. Additional tempering cycles and careful use of alloying elements can also be used to influence the microstructure and final behaviour of the tool steel. This has been studied through a comparison of wear rates and modes, as well as lab-scale trimming trials However; the analysis that exists today fails to bridge the gap between lab scale analysis and industrial performance.

This study aims to set the foundation for characterizing tool steels for further predictive analyses. It will also create a link between existing fundamentals, such as uni-axial tensile and compression tests and industrial applications.

Chapter 3

Experimental Work

3.1 Materials

Three tool steels are used in the course of this work. Uddeholm produced two of the materials used in this investigation, Carmo and Caldie. The chemical composition of the three steels is given in Table 3.1, with the C and Cr contents emphasized.

Table 3.1: Material composition of three tool die steels in wt% [40, 41, 42].

Material	**C**	**Cr**	**Si**	**Mn**	**Mo**	**V**
D2	**1.4 - 1.6**	**11 - 13**	0.1 - 0.6	0.1 - 0.6	0.7 - 1.2	0.5 - 1.10
Carmo	**0.6**	**4.5**	0.35	0.8	0.5	0.2
Caldie	**0.7**	**5.0**	0.2	0.5	2.3	0.5

3.2 Heat treatment

The heat treatments were obtained thorough analysis of the standards and data sheets available for all three tool steels based on the final hardness. Specifically, the heat treatment of D2 is expected to have followed the ASTM standard A681 [40]. The heat treatment of Carmo is based on the hardness specifications of 58 $\pm$ 1 HRC and the data sheet given in reference [41]. The heat treatment of Caldie is based on the hardness specifications of 61 $\pm$ 1 HRC and the data sheet given in reference [42]. All three tool steels were produced by

an initial preheating, followed by austenitization and one or more temper treatments. The results of this analysis are compiled in Table 3.2.

Table 3.2: Heat treatment of three tool steels based on their specifications [40, 41, 42].

Material	Preheat	Austenization	Temper
D2	816°C	996-1010°C (10-20 mins)	Single 204 °C
Carmo	600-700°C	900°C (30-45 mins)	Double 250°C
Caldie	600-650°C then 850-900°C	1050°C (30 mins)	Triple 540°C

3.3 Microscopy

Samples for microscopy were cut using wire EDM. The specimens were ground using 120, 240, 320, 600, 800, 1200 grit abrasive papers. The specimens were then polished with 3μm and 1μm diamond solution until the surface was scratch free and of mirror quality. The D2 specimens were etched with 4% Nital to reveal its microstructure. The Carmo and Caldie specimens were etched with a mixture of one part 4% Nital to two parts Picral (4% picric acid).

A light optical microscope (OM, Olympus GX51) was used to study the microstructure at lower magnifications. A scanning electron microscope (SEM, FEI Quanta 200 FEG) was used to study the microstructure and fracture surfaces at higher magnifications as well as in the study of the fracture and wear surfaces. Both secondary electron and backscattered electron detectors were used. An energy dispersive x-ray spectrometer (EDS, Octane Plus SDD) featured with the SEM was used to measure the chemical composition of the carbides contained in the microstructure.

3.3.1 Carbide Analysis

Images were taken at 4000X magnification using SEM, BSE. Images were imported into photo editing software. Each carbide was selected and then filled with colour. A sample of this is shown in Figure 3.1. The image was then imported into ImageJ, where

the threshold was set to isolate the coloured areas. Measurements were taken of the widths, lengths, and area fraction for each of the carbides.

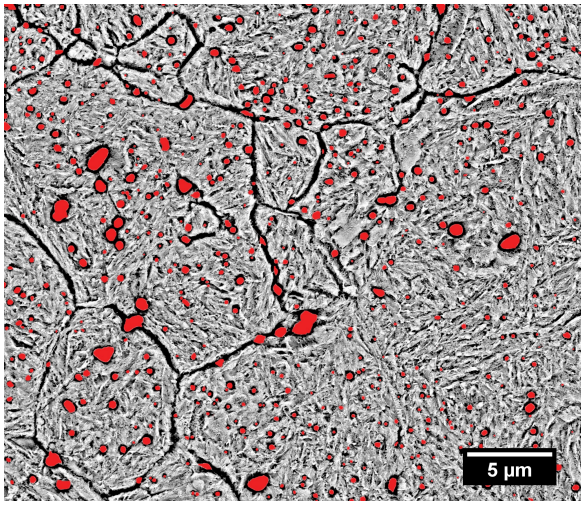

Figure 3.1: BSE Image of Carmo with carbides highlighted, SEM 4000X

3.4 Mechanical Testing

3.4.1 Compression Tests

Uniaxial compression tests were performed at room temperature at a rate of 0.1mm/min to maintain a quasi-static loading condition. The tests were performed using an MTS Universal Testing machine. A 600kN load cell was used to record the load throughout the test. Tests were conducted on all three materials in the same testing machine. Samples were cleaned with acetone, dried, and then spray painted with a fine matte white and black speckle pattern on the same day the test was performed to ensure the paint was sufficiently ductile not to crack during the test. A 2D DIC system was used to capture and process images and was used as a digital extensometer.

The cylindrical specimens had a diameter of 8mm. Samples had a length of 12mm, for an aspect ratio slightly below 1.5:1. This ratio is recommended per the ASTM standard E9 [38]. The samples were cut using wire EDM. The specimens rested between two cylindrical disks of D2 which acted to prevent indentation to the plates used to perform the compression tests. The flat surfaces of the compression specimens were polished to a

mirror finish using 3μm diamond polishing solution. Nikal, a nickel based lubricant was used.

3.4.2 Tensile Tests

Uniaxial tensile tests were performed at room temperature at a rate of 0.1mm/min to maintain a quasi-static loading condition. The tests were performed using an MTS Universal Testing machine. A 50kN load cell was used to record the load throughout the test. Samples were prepared in a similar fashion to the compression tests; they were cleaned, and spray painted with a white and black speckle pattern the day of the test. A 2D DIC system was used to capture and process images as a digital extensometer. The samples were cut using wire EDM to the shape shown in Figure 3.2a, with a thickness of 1.5mm.

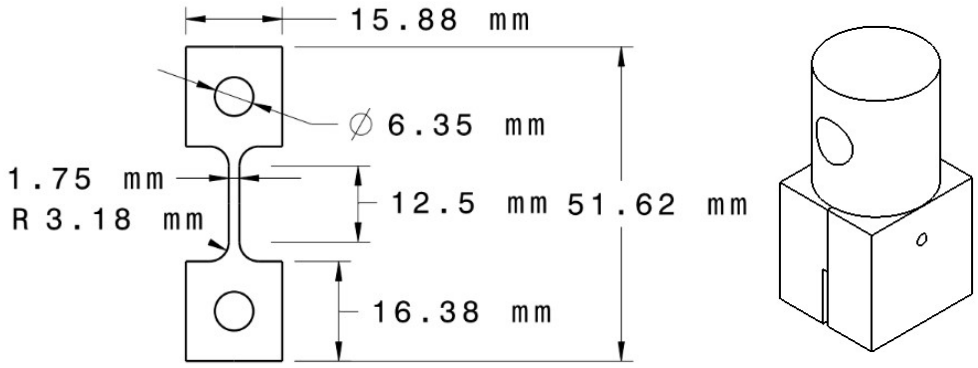

(a) Tensile test specimen [43]

(b) Grip used

Figure 3.2: Drawings used in execution of tensile tests

Due to the high hardness of the materials being tested, custom grips were fabricated out of stainless steel 316 to hold the samples in place, shown in Figure 3.2b.

3.4.3 Compression Shear Tests

Compression shear tests were performed using the same methodology as the uniaxial compression tests. The geometry shown in Figure 3.3 and described by Dorogoy et al. was used [44]. The samples were cleaned and taped to ensure that the spray paint only coated the gauge area.

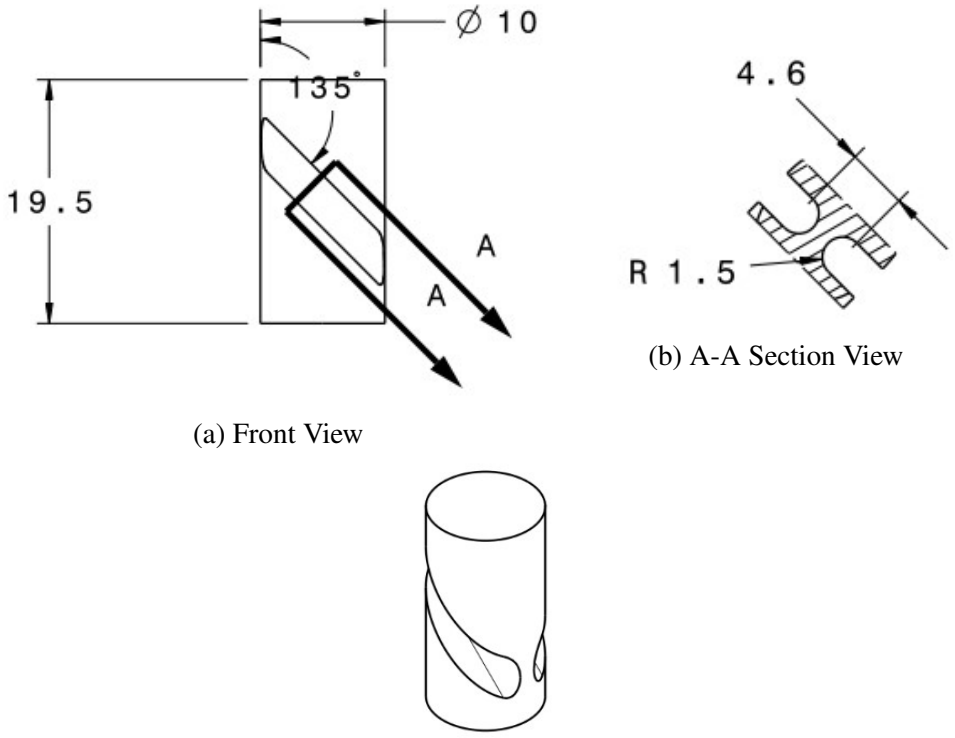

(a) Front View

(b) A-A Section View

(c) Isometric View

Figure 3.3: Drawings of shear compression tests

3.4.4 Side Press Tests

Side press tests were also conducted on all three tool steels. The set up was similar to that of the compression tests. The cylindrical specimens had a diameter of 8mm and a length of 12mm and were produced by wire-EDM. In this test, the sample was rotated, and compressed in the radial direction as opposed to the axial direction as in the compression tests. The tests were performed without lubrication and the test specimens were not ground or polished. The specimens were centered in the machine and on the platen prior to the start of testing. One test, performed on D2 steel specimen, was interrupted after the first cracks formed to investigate the initiation and propagation of cracks through this cylindrical geometry.

3.5 Trimming of Tool Steels in Industrial-Scale Press

Die inserts were tested using an industrial-scale, semi-production facility. A 127-mm wide coil of uncoated DP980 is fed into a decoiler, leading to a straightener/feeder, into a mechanical press. Die insert pairs consisted of D2 upper with D2 lower inserts, and Carmo upper with TiCN coated Caldie as the lower inserts. White light interferometry measurements were taken using a surface profilometer, WYKO NT-1100, in VSI (vertical scanning interferometry) mode. These measurements are used to create a 3D profile of the specimen surface which is particularly useful in wear measurements. In this case, it is used to identify the material loss on the die edge.

Measurements were taken after 40,000 trimming cycles. Five regions were chosen at equal intervals along the trim edge for both Carmo and Caldie inserts. Each region was approximately 5mm long. Measurements of the trim edge profile of each region were taken on both the sliding plane and the impact plane, as indicated in Figure 2.11.

3.5.1 Wear Rate Calculations

Height measurements as well as the co-ordinates for each section were exported from the WYKO NT-1100. These measurements are 1 pixel, or approximately 0.0015mm, apart. An area located away from the trim edge was defined as an undamaged area; this area is generally characterized by its relative flatness and the appearance of grinding marks. An image of a profile with the undamaged area identified is given in Figure 3.4a. The height of every point within the undamaged area is averaged and subtracted from the height of all the points in the region of interest. The points within the undamaged area are not considered in the wear calculation. Points which measured above the average of the undamaged area also are not considered and are cut off. This leaves the area lost due to wear. These transformations are shown in Figure 3.4b.

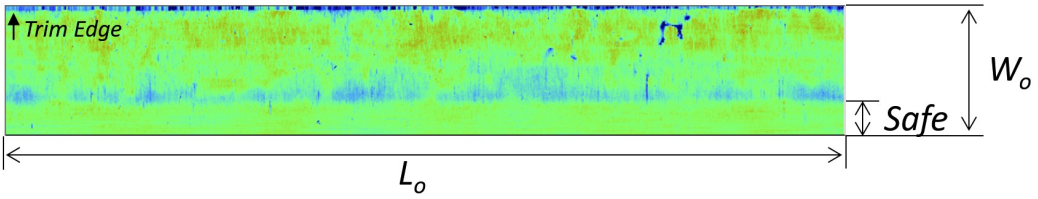

(a) Profile of the trim edge identifying the safe/undamaged area. Areas with volume loss are shown in dark blue. Width identified as W_0, Length as L_0.

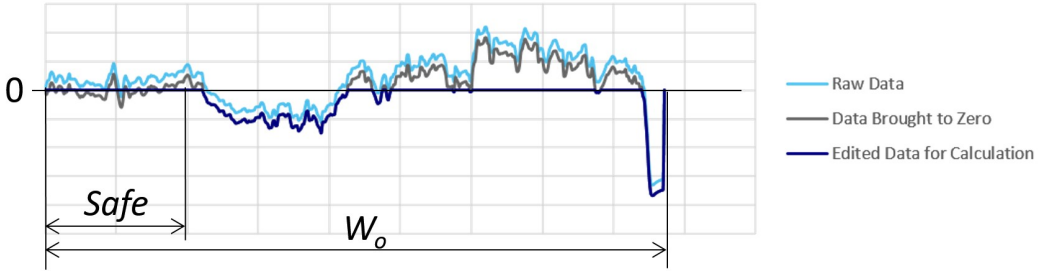

(b) Example of one line of height measurements graphically depicting the transformations done to the raw data.

Figure 3.4: Images showing the process of capturing the profile of the trim edge and transforming the height data for calculation of the volumetric wear loss.

The height measurements are segregated into lines, where each line represents the height measurements for one pixel along the length. Each line is then integrated using the trapezoidal method. The area represented by the integration can be seen as shaded in Figure 3.5, and is denoted by A_i in Equations 3.1 and 3.2.

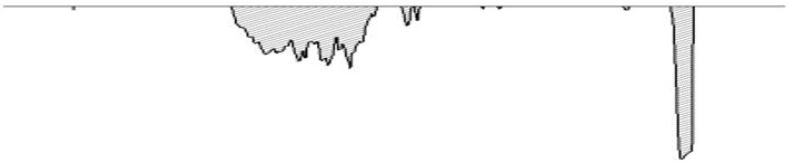

Figure 3.5: Shaded area showing area used in integration to determine wear loss.

The areas are then summed, which is used to give a volume loss for the section, as shown by Equation 3.1. The n value is the number of lines used in the summation, calculated by dividing the region length by the space between measurements (0.0015mm). In this case, with a region length of 5mm, the n value is approximately 3300. As the die is 12.7cm in length, a weighted volume loss is then defined by Equation 3.2.

$$V = \sum_{i=1}^{n} A_i \tag{3.1}$$

$$V_w = \sum_{i=1}^{3300} A_i \frac{127000}{L_0} \tag{3.2}$$

Chipping is also taken into consideration. In areas where chipping can be seen as typical wear behaviour across multiple sections, there was no change to the analysis. In Carmo, where large chipped areas could be seen, but it did not appear to be the typical wear behaviour, the chipping was treated as a deviation factor. The volumetric wear loss was calculated with and without the large chips, and then an average was taken, with the averages of the wear loss with and without chipping used to define the error bar. A more in depth look into the result of this analysis can be seen in Fig 3.6.

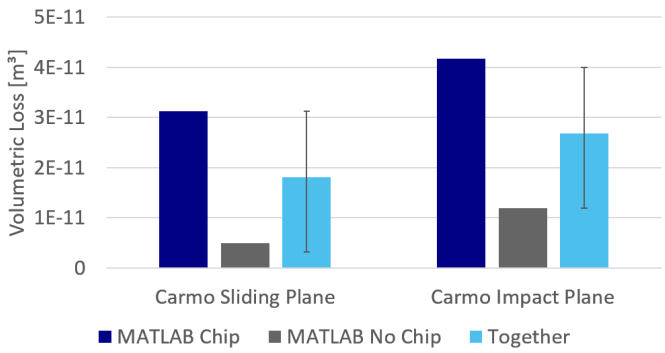

Figure 3.6: Bar chart showing magnitude of effect of chips on wear loss calculation and resultant error bar.

Chapter 4

Experimental Results

4.1 Microstructure Analysis

Typical SEM images of the three tool steels are shown in Figure 4.1. The carbides are represented by darker or lighter areas in the overall matrix. It is of interest that the carbides in Figure 4.1a can develop to over 100μm in length and appear to band together. They are not well distributed across the microstructure. Even at higher magnifications, as in Figure 4.1b, some of the carbides appear larger and have formed in a band. This is in direct contrast to the other two materials, Carmo and Caldie, where the carbides are not visible at the lower magnification, and there are no carbides which exceed 2μm in length.

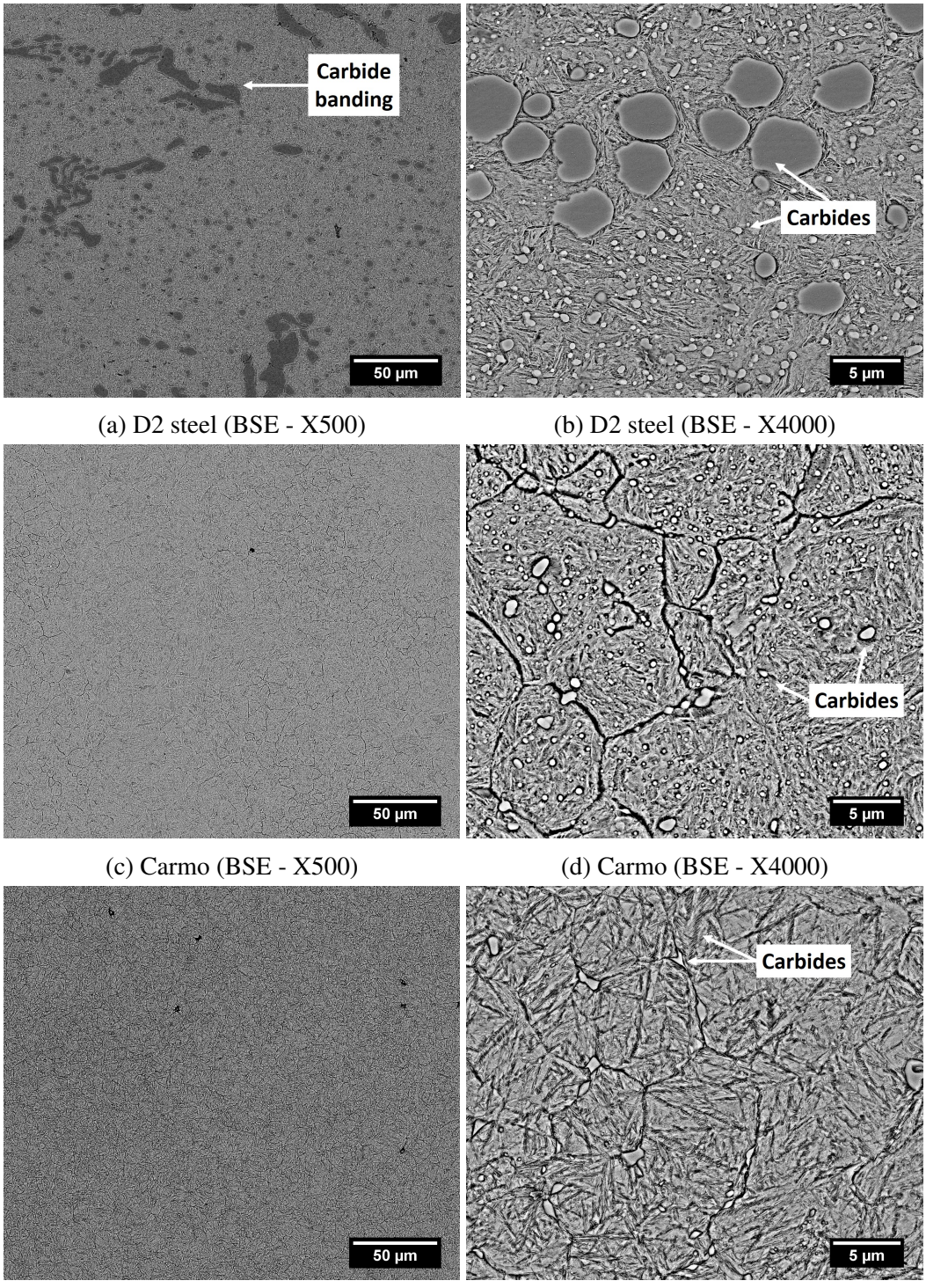

(a) D2 steel (BSE - X500)

(b) D2 steel (BSE - X4000)

(c) Carmo (BSE - X500)

(d) Carmo (BSE - X4000)

(e) Caldie (BSE - X500)

(f) Caldie (BSE - X4000)

Figure 4.1: Images of tool steel microstructure

Nano-sized, tempering carbides have been identified by Rehan [5], and can be seen in the Caldie microstructure captured in Figure 4.1f. Figure 4.2 depicts an image of the Caldie microstructure at a higher magnification to highlight these particles.

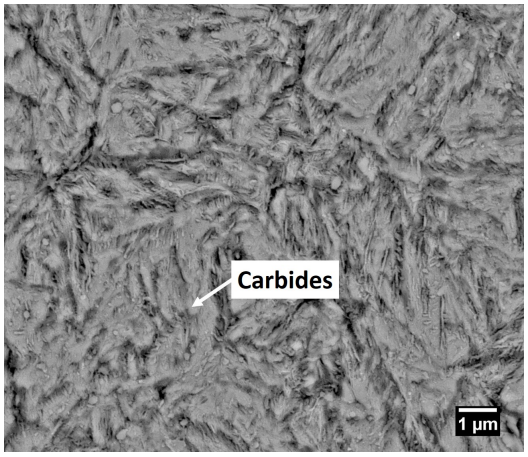

Figure 4.2: Caldie SEM BSE X10000 etched microstructure

Two very simple metrics for comparing carbide distribution within a matrix are shown in Figure 4.3. Of note is the relatively small % area taken up by carbides when compared to the number of carbides in the same area. This is also reflected in Figures 4.4 and 4.5.

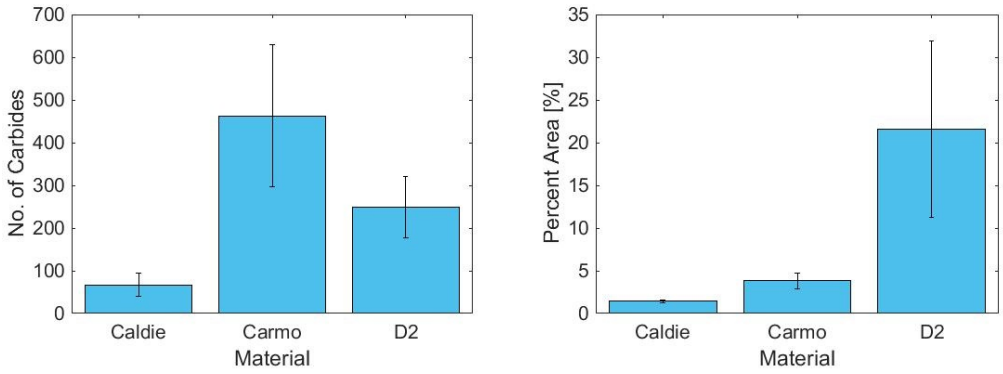

(a) Number of carbides (b) Percentage area

Figure 4.3: Carbide distribution graphs for a 990μm^2 area

Figures 4.4 and 4.5 show the distribution of carbides as they can be measured in Figure 4.1b,d, and f. This does not include the nano-sized particles in Caldie. This explains the relatively small number of carbides captured for Caldie. Figures 4.4 and 4.5 quantify what is shown in Figure 4.1, that there is a large range in carbide sizes in D2, and a more

homogenous structure in Carmo and Caldie. These figures also show a very high number of equally shaped, micron-sized particles in Carmo, compared to Caldie and D2.

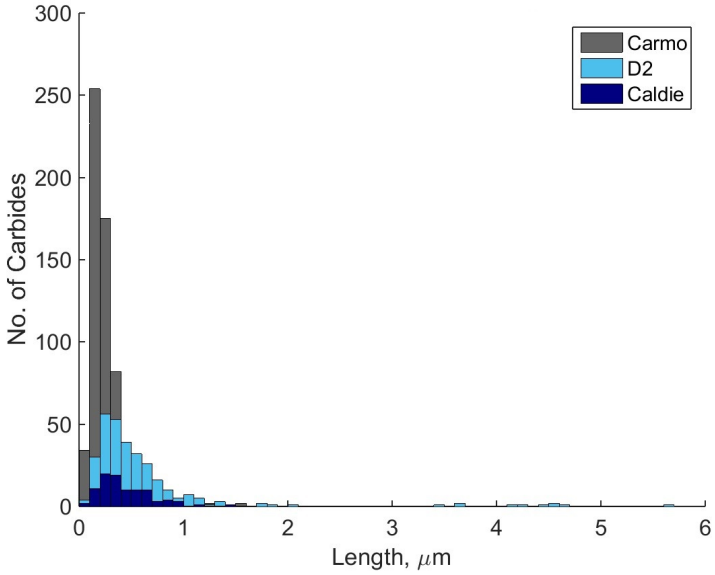

(a) Distribution of carbide lengths

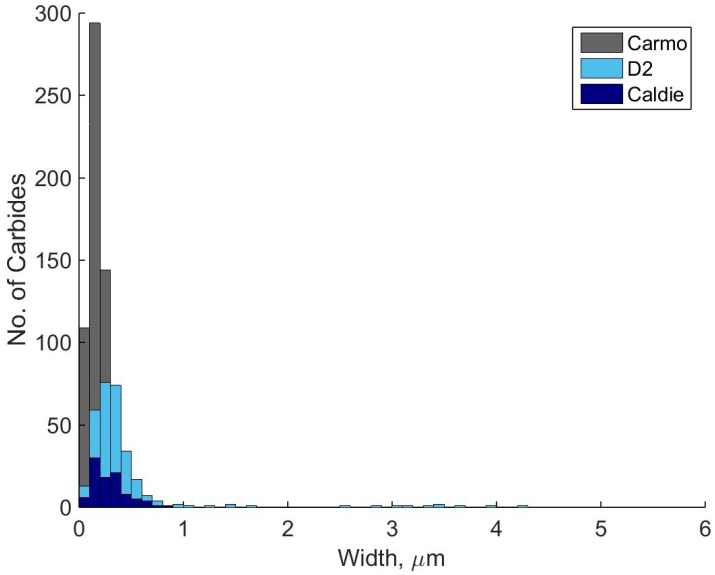

(b) Distribution of carbide widths

Figure 4.4: Carbide distribution graphs for a $990\mu m^2$ area

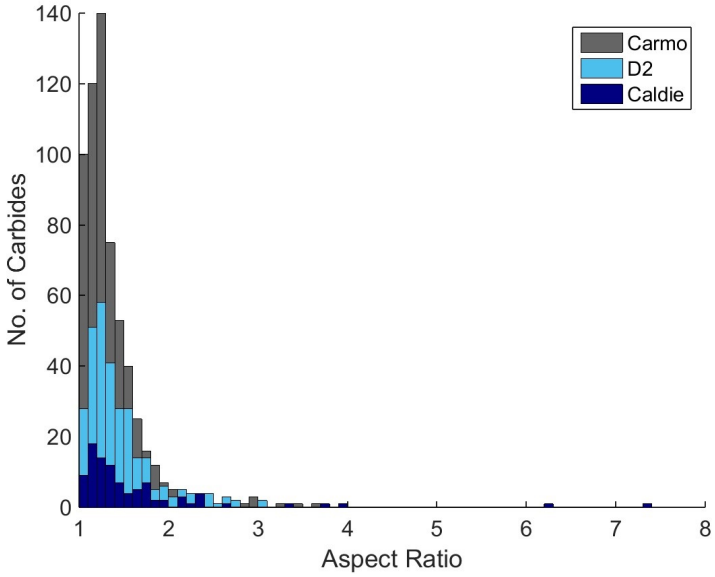

Figure 4.5: Distribution of carbide aspect ratio for a 990μm^2 area

4.2 Compression Tests

The stress-strain curves for all three materials subject to compressive loads are shown in Figure 4.6.

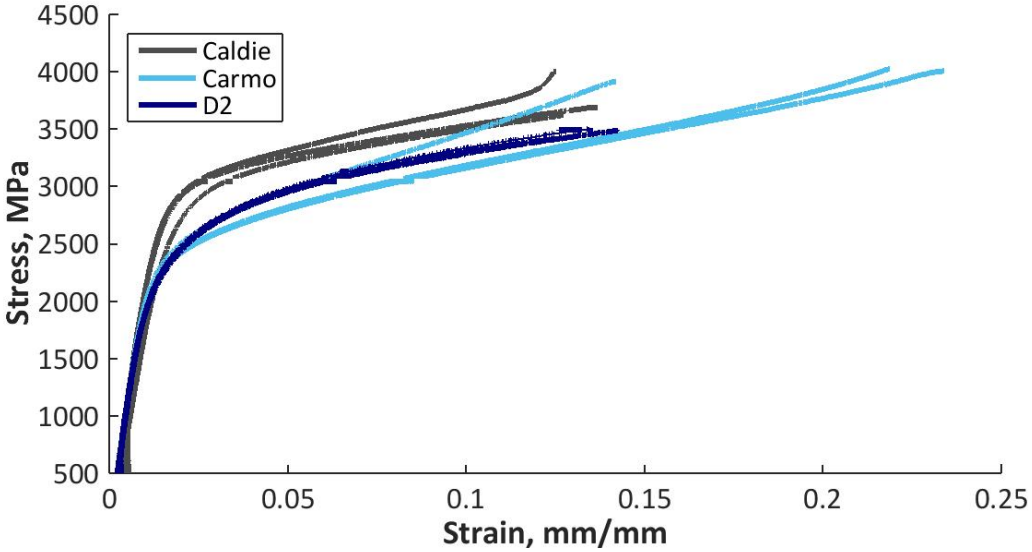

Figure 4.6: Compression test results

As the elastic properties of steel are rather well known, the elastic modulus was used to validate the strain results obtained through DIC analysis. The elastic moduli, or the slope of the elastic portion of the stress-strain curve, was found to be 216 ± 5 GPa, 215 ± 6 GPa and 206 ± 20 GPa for D2, Carmo, and Caldie, respectively. The yield strengths in D2, Carmo, and Caldie in compression are expected to be approximately 2050, 2000, and 2430 MPa, respectively based on their material data sheets [42, 41, 45]. This is fairly consistent with the values obtained from compression testing and are presented in Table 4.1. The yield stress for Caldie in compression is higher than that in tension.

The fracture stresses in compression for D2, Carmo, and Caldie are presented in Table 4.1.

Table 4.1: Mechanical properties of three tool steels in compression.

Material	**Elastic Modulus**	**0.2% Yield Stress**	**Fracture Stress**
D2	216 ± 5 GPa	2008 ± 42 MPa	3425 ± 90 MPa
Carmo	220 ± 2 GPa	2063 ± 34 MPa	4128 ± 156 MPa
Caldie	206 ± 20 GPa	2542 ± 58 MPa	3912 ± 259 MPa

Figure 4.7a depicts two fracture surfaces which were identified on the fractured D2 specimen. One surface, which appears shiny is congruent with quasi-static fracture along the shear band. The other surface is suspected to have been formed post-quasi-static fracture and appears dull. It is thought that the post-quasi-static fracture surface was formed as the sample impacted the platen: as the fractured pieces separated, and the final fracture occurred, the pieces contact the opposite platen and become fused to the surface. This suggests a high strain rate impact. This would not be due to an inconsistent crosshead speed, but rather the high speed at which fracture occurs. One such sample can be seen in Figure 4.7b, where a fractured piece of the sample which originally contacted the upper platen, can be seen to be embedded in the lower platen, with a vertical crack running through it. The vertical crack is not associated with fracture along the shear band.

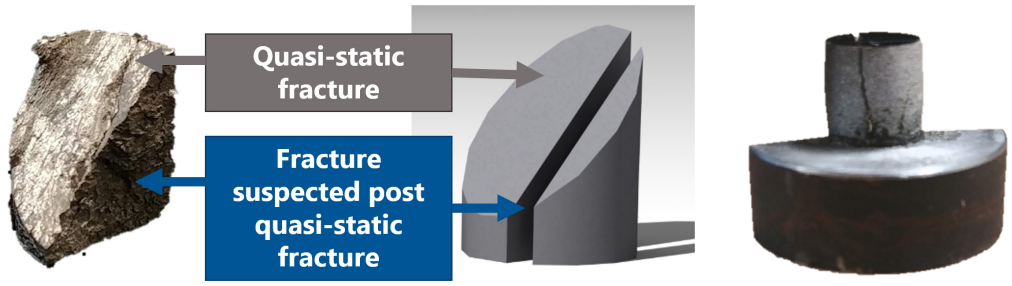

(a) Two fracture surfaces which exist on some tested samples

(b) Sample embedded in opposing platen surface

Figure 4.7: Fracture surfaces of D2 specimens tested in compression

Back scattered electron images showing samples of magnified fracture surfaces can be seen in Figures 4.8 to 4.10. Figures 4.8a and 4.8b show the typical compressive fracture surfaces of D2. The clustering and cleavage fracture of large primary carbides can be seen, adjacent to ductile fracture of the matrix. This fracture surface is shiny at the macro level. Figures 4.8c and 4.8d are SEM images of the fracture surface in the area that appears dull in Figure 4.7a. Bands of broken carbides can be seen clearly on this surface and it appears to be distinct from the other surface shown.

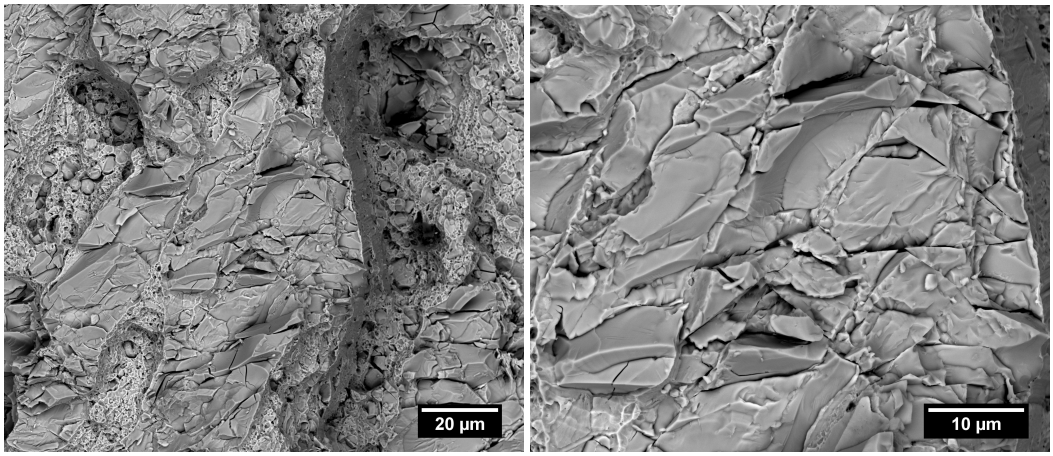

(a) D2 steel (BSE - X1000) (b) D2 steel (BSE - X2500)

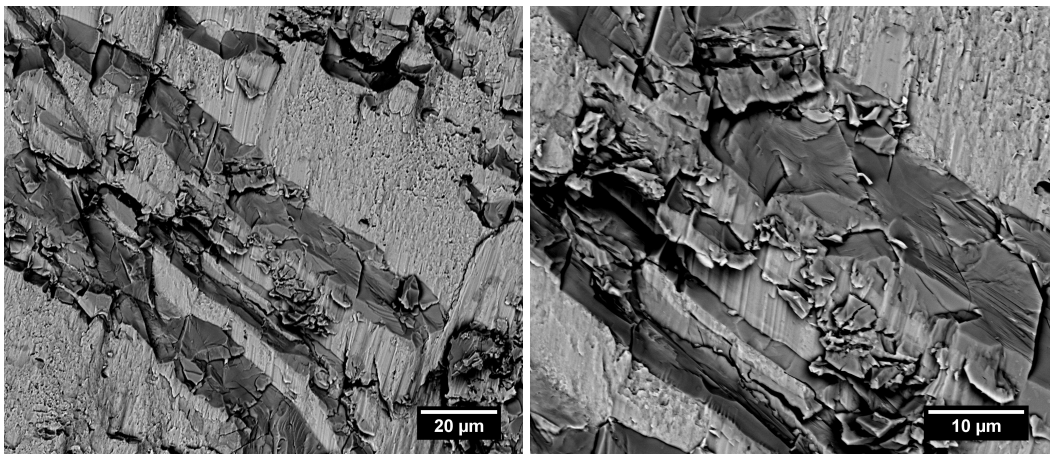

(c) D2 steel (BSE - X1000) (d) D2 steel (BSE - X2500)

Figure 4.8: SEM images of fracture surfaces on D2 specimens tested in compression

Figure 4.9 depicts the fracture surface of the Carmo compression samples. There appears to be two distinct types of fracture. Figures 4.9a and 4.9b show an interface between the two types of areas. These images were taken closer to the edge of the sample. The area at the top of this image appears darker and can be seen to be more grainy in comparison to the area in the lower part of the image. The appearance of the upper portion can be seen in other areas of the fracture surface. The difference in colour does not appear to be due to difference in composition, per EDS analysis. Figure 4.9c and the lower portion of Figure 4.9b have very flat surfaces that do not show a lot of detail. Figure 4.9c shows clear cleavage fracture planes. Figure 4.9d depicts similar cleavage planes with much more detail.

This detail could possibly be associated with quasi-cleavage fracture, with ridges forming within the fracture plane.

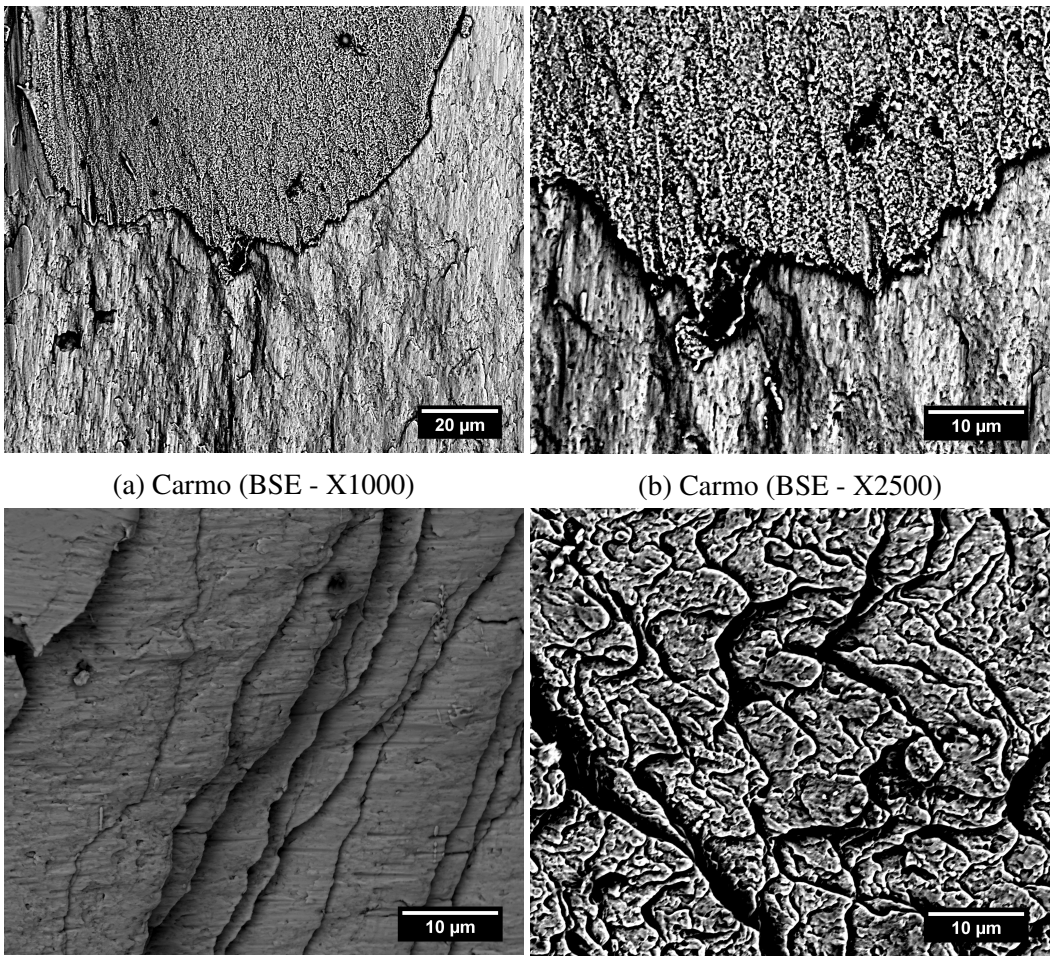

(a) Carmo (BSE - X1000)

(b) Carmo (BSE - X2500)

(c) Carmo (BSE - X2500)

(d) Carmo (BSE - X2500)

Figure 4.9: SEM images of fracture surfaces on Carmo specimens tested in compression

Figure 4.10 shows the typical fracture surfaces for Caldie in compression. Figure 4.10a shows primarily quasi-cleavage fracture. This is in addition to planes that can be seen cutting diagonally through the image. Further cleavage planes can be seen in Figure 4.10b. Both appear very similar to the Carmo fracture surfaces.

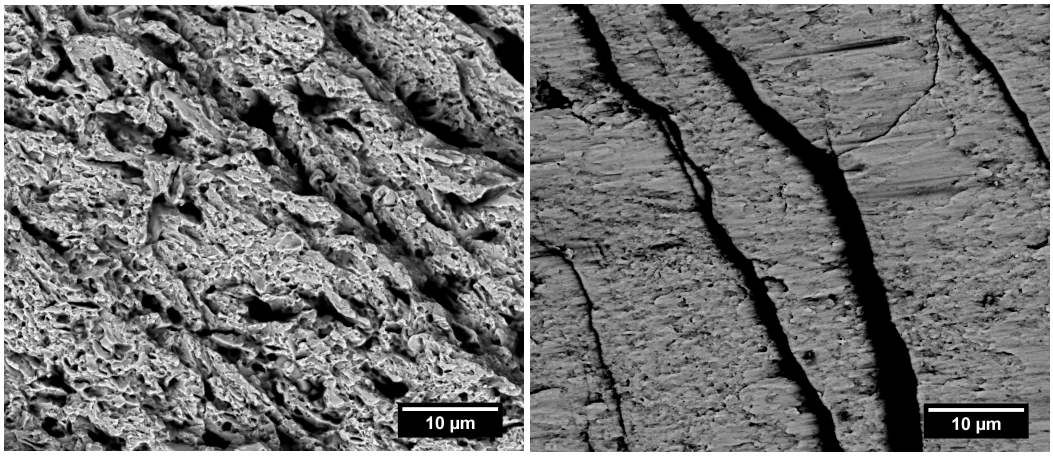

(a) Caldie (BSE - X2500) (b) Caldie (BSE - X1000)

Figure 4.10: SEM images of fracture surfaces on Caldie specimens tested in compression

4.3 Tension Tests

The stress-strain curves for all three materials are shown in Figure 4.11. A callout is made to highlight the consistency in the data throughout this plot.

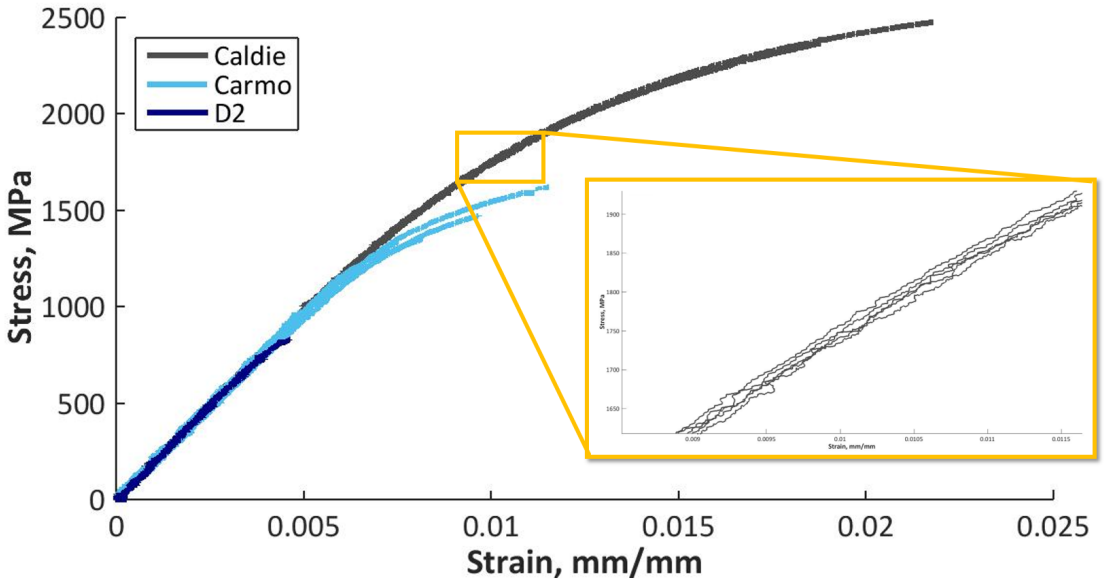

Figure 4.11: Tensile test results

As the elastic properties of steel are well known, the elastic modulus was used to validate the strain results obtained through DIC analysis. The elastic moduli, or the slope

of the elastic portion of the stress-strain curve, was found to be 201 ± 9 GPa, 190 ± 2 GPa and 196 ± 4 GPa for D2, Carmo, and Caldie, respectively. These values are what would be expected of the material, and thus speak to the validity of the results.

D2 showed no evidence of plastic deformation prior to fracture based on the stress/strain curves obtained. Carmo samples fractured in or just beyond the elastic portion. Caldie displayed a small amount of plastic deformation, which can be expressed by a 0.2% yield stress of 1946 ± 26 MPa. Approximately 1% plastic strain can be observed.

The fracture stresses in tension for D2, Carmo, and Caldie are presented in Table 4.2. The results show a higher strength and deformation in Caldie than the two other materials.

Table 4.2: Mechanical properties of three tool steels in tension.

Material	**Fracture Stress**	**Elastic Modulus**	**0.2% Yield Stress**
D2	816 ± 65 MPa	201 ± 9 GPa	N/A
Carmo	1267 ± 192 MPa	190 ± 4 GPa	N/A
Caldie	2219 ± 196 MPa	196 ± 4 GPa	1946 ± 26 MPa

Back scattered electron images showing the overall fracture surface as well as a typical magnified surface can be seen in Figure 4.12.

The overall fracture surface shown in Figure 4.12a depicts a very consistent cleavage fracture surface as a result of D2 failure in tension. Cleavage planes are present and there is no ductile lip. When looking at a magnified image at any point of the D2 tensile fracture surface, such as in Figure 4.12b, it is even more evident that the dominant fracture mechanism is brittle fracture. This is shown in the feathering and cracking of the large primary carbide as well as the evidence of cleavage planes among the smaller carbides. This magnified view also shows evidence of ductile fracture within the matrix.

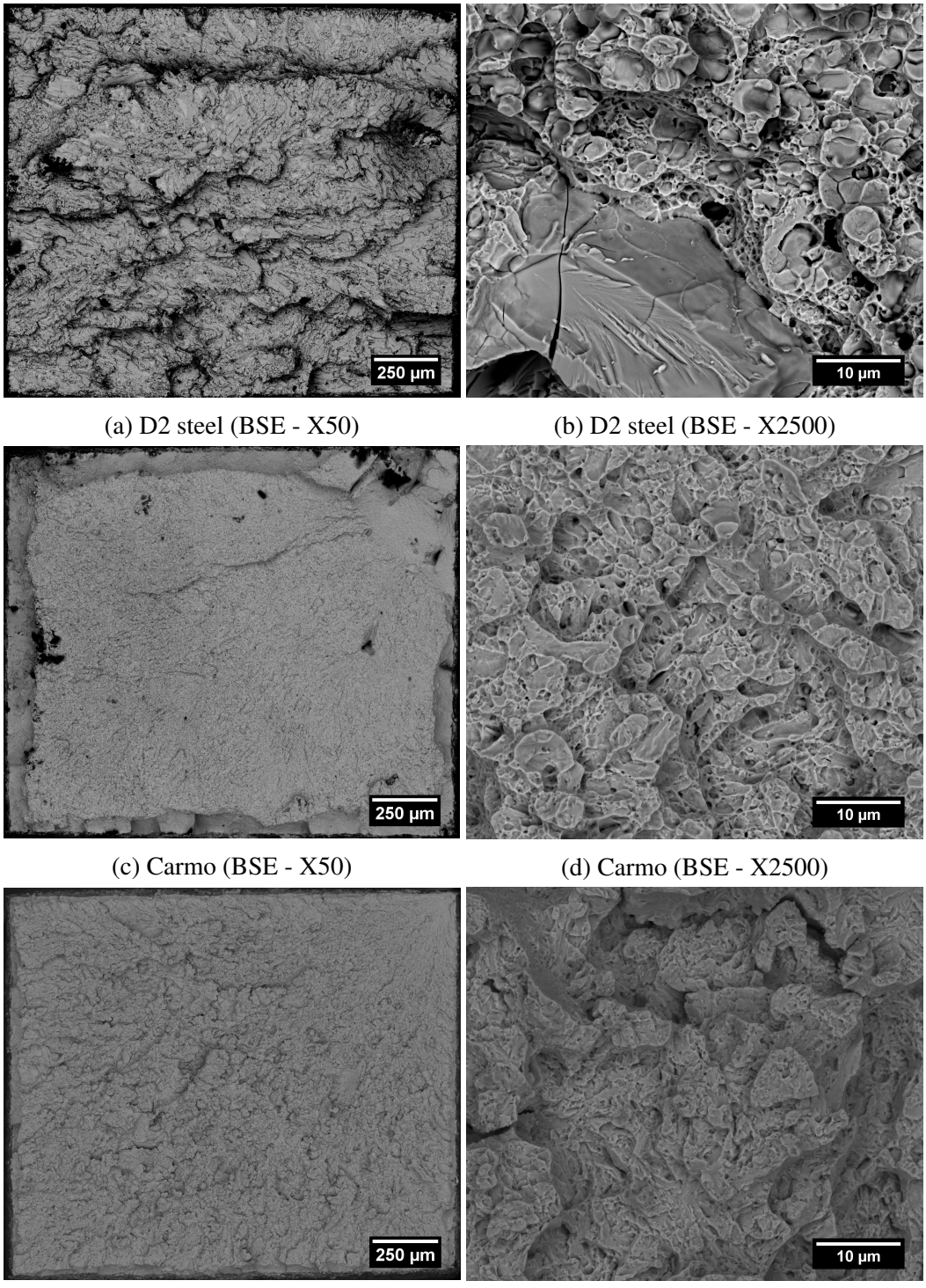

(a) D2 steel (BSE - X50)

(b) D2 steel (BSE - X2500)

(c) Carmo (BSE - X50)

(d) Carmo (BSE - X2500)

(e) Caldie (BSE - X50)

(f) X2500 Caldie BSE

Figure 4.12: SEM images of fracture surfaces on specimens tested in tension

Figure 4.12c shows that the fracture surface of Carmo in tension formed ductile lips, evidence that the fracture was not entirely brittle as one would expect with a tool steel.

Figure 4.12d shows the typical fracture surface of Carmo in tension from the center of the fracture surface. This surface shows a mixture of ductile fracture, as well as the ridges which can be associated with quasi-cleavage fracture. As in the D2 sample, small carbides can be seen within the cup and cone fracture which is a typical morphology of ductile fracture. There are other areas of interest on the surface depicted in Figure 4.12c, as well as in other Carmo tensile fracture surfaces studied. These are discussed below in Section 4.3.1.

Figure 4.12e depicts the fracture surface of Caldie in tension. It can be seen in this image that the fracture initiated on the top right corner and the fracture then radiated, until reaching a sort of equilibrium as evidenced by the uniform fracture surface. A minimal ductile lip can be noted around the edges. Figure 4.12f depicts a very typical fracture surface. The images taken in the center of this sample look identical to images taken near the initiation point. This surface shows quasi-cleavage fracture, similar to the typical fracture surface in the centre of the Carmo sample shown in Figure 4.12d. The ridges that define this fracture as quasi-cleavage are better defined at higher magnifications, as shown in Figure 4.13. There are small carbides present on the fracture surface of all three materials.

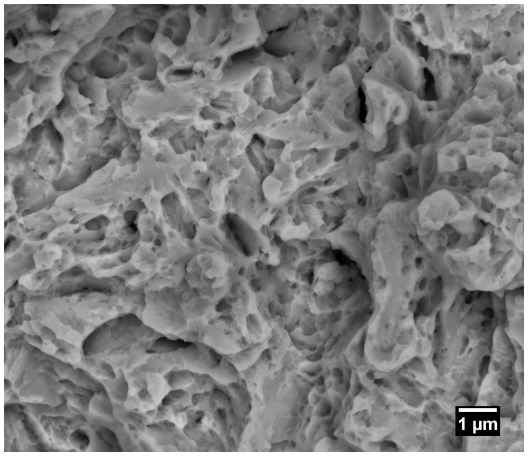

Figure 4.13: SEM image of Caldie tensile fracture surface (BSE - X10000)

4.3.1 Carmo Tensile Fracture

There were several locations of interest found on the Carmo tensile fracture surface. The production of this sample resulted in the formation of several impurities which likely contributed to the sample fracture. Thus, these impurities are not seen on the etched surface, but can be found on the fracture surface.

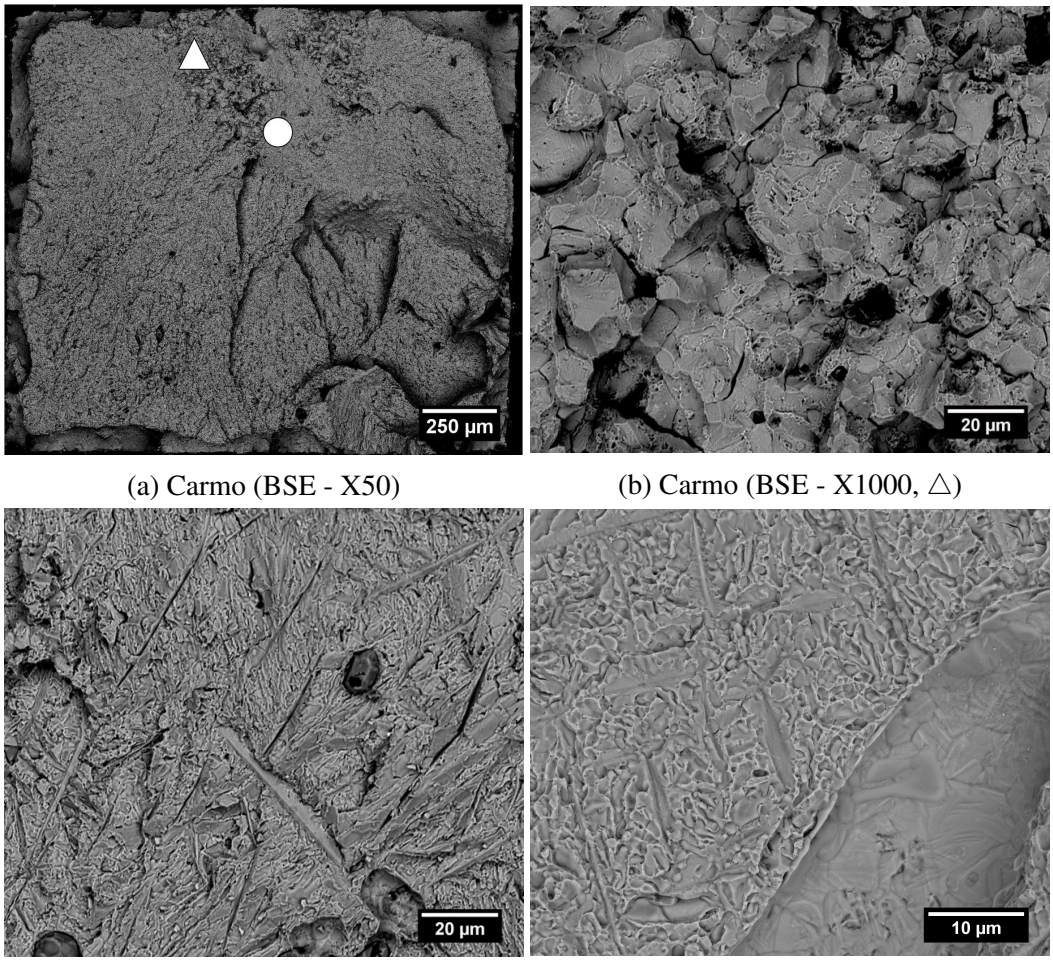

(a) Carmo (BSE - X50)

(b) Carmo (BSE - X1000, △)

(c) Carmo (BSE - X1000, ◯)

(d) Carmo (BSE - X2500)

Figure 4.14: SEM images of fracture surfaces on Carmo specimens tested in tension

The areas of interest exist across several samples. Figures 4.14b to 4.14c belong to the same sample, and are represented by △ and ◯ symbols, respectively, on Figure 4.14a while Figure 4.14d is a magnified image of the area located at the top right hand corner of Figure 4.12c. Figure 4.14b is an example of the intergranular fracture that could be seen on more than one tensile fracture surface for this material. The EDS analysis showed that the

area revealed by the intergranular fracture is composed of 90-95 wt.% Fe, which is slightly higher than a typical location on the matrix, which is composed of 85 wt.% Fe. This area also does not appear to have any carbides showing in the fracture surface, which is atypical for this material.

Concentrations of vanadium and chromium can be seen in Figure 4.14d. They appear as straight lines, often in hatchmark patterns and can have a raised appearance. This region of concentrations is located beside an area which appears to have been occupied by a much larger impurity which was removed through fracture, or is a result of a large void. This area features a primary carbide which is larger than those seen in the etched microstructure; measuring approximately 10 μm long. These concentrations can be seen across multiple fracture surfaces. These concentrations have between 8 and 10 wt.% V, and between 5 and 19 wt.% Cr, whereas the typical location has less than 1wt.% V and approximately 5wt.% Cr. Another area with these same hatch marks is shown in Figure 4.14c. Embedded MnS, shown as darker, spherical areas in the image, appear in these same regions. It can also be seen that impurities have been removed from the fracture surface in the bottom right corner of this image. EDS of the area confirms the presence of MnS, reinforcing the assumption of spherical impurities.

4.4 Compression Shear Tests

Back-scattered electron images showing the fracture surfaces at the top or bottom and the center of the dfracture surface shown in Figure 4.15, where the top of the fracture surface would be the top of the image shown. The images are shown in Figure 4.16. The fracture has a direction to it, as would be expected of a sheared sample.

Figure 4.15: Typical Shear Compression Fracture Surface

An image of a typical fracture surface can be seen in Figure 4.15. The fracture surface appears shiny, but not entirely flat. Even at a macro scale, there is a directionality to the fracture. The fracture of the D2 sample shown in Figure 4.16a shows definite directionality. The large carbides typical of D2 can be seen in this image as darker areas. Shear ductile fracture can be seen at the bottom of the image. Most of the fracture surface appears to look more like the result of galling than of fracture. Figure 4.16b captured at the edge of the sample, is representative of the surface without the same featureless sliding phenomena. In this image, the carbides appear as dark areas. It shows the fracturing of the carbides perpendicular to the sliding direction. The features are also very similar to Carmo in compression, as shown in Figure 4.9b.

The fracture surface of Carmo in shear compression appears very different when comparing the edge of the sample to the middle of the sample. The middle of the fracture surface is captured by Figure 4.16c. It shows ridges which are consistent with quasi-cleavage fracture. This is consistent with the surface captured by Figure 4.9d, and both can be associated with quasi-cleavage fracture.

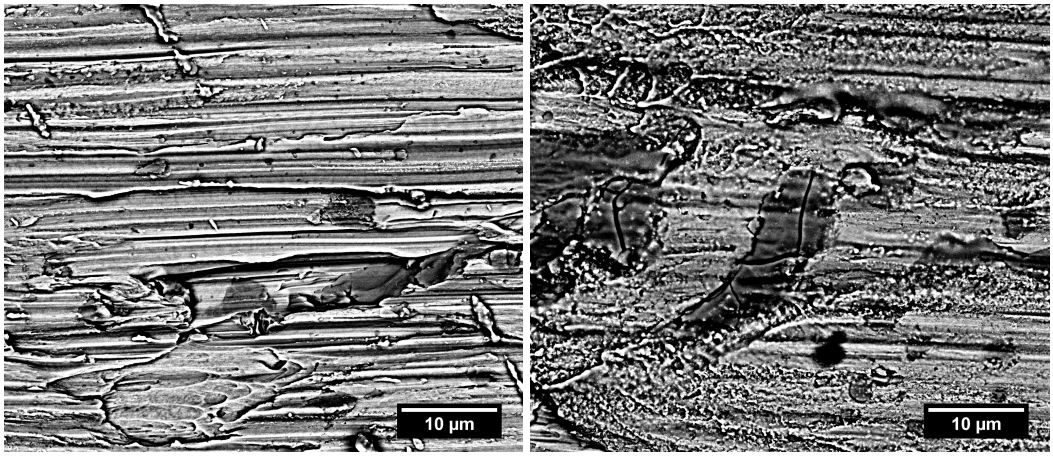

(a) D2 (BSE - X2500) (b) D2 (BSE - X2500)

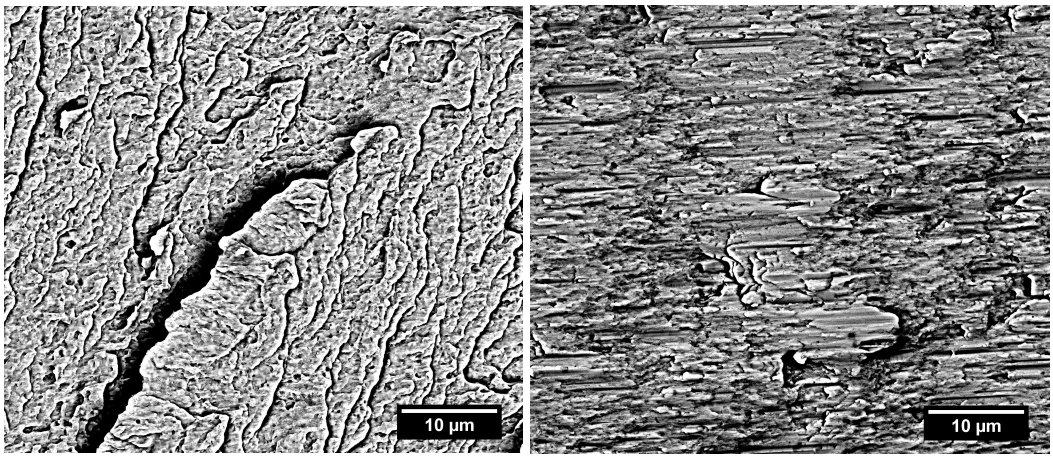

(c) Carmo (BSE - X2500) (d) Carmo (BSE - X2500)

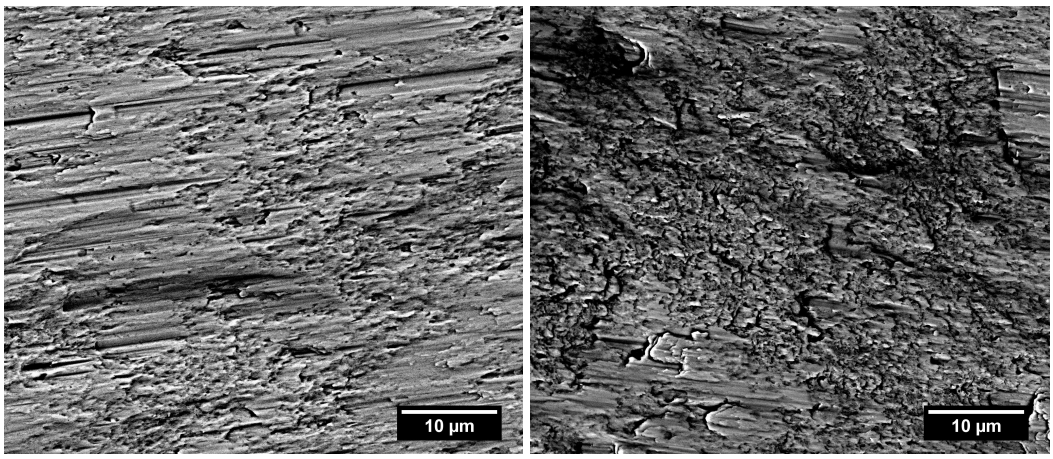

(e) Caldie (BSE - X2500) (f) Caldie (BSE - X2500)

Figure 4.16: SEM images of compression shear fracture surfaces on shear specimens tested in compression

Figure 4.16d shows two different types of surfaces. There are areas which appear similar to Figure 4.16b, which appear featureless outside of sliding marks in the direction of fracture, likely due to transfer of material across fracture surfaces. The other areas appear grainy in texture. This is similar to the Caldie compression shear fracture surface shown in Figures 4.16e and 4.16f. Caldie's fracture surface has both the flat and grainy areas across its surface, making it more consistent than D2 and Carmo. A higher magnification image of the grainy areas in Figure 4.16f can be seen in Figure 4.17. The lighter, spherical areas of the grainy area appear to be carbides. This surface was likely formed out of a mixture of ductile and brittle fracture.

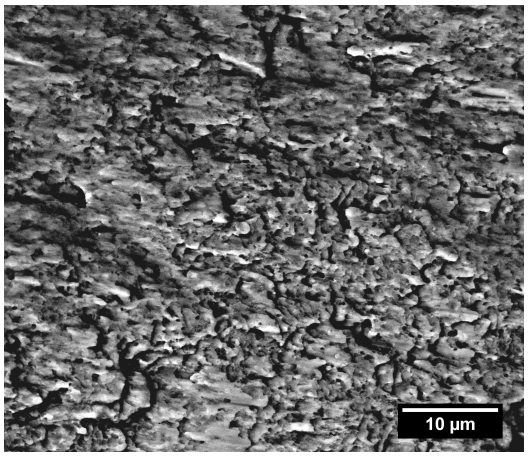

Figure 4.17: SEM image of Caldie compression shear fracture surface. X5000 BSE

4.5 Side Press Tests

One D2 test was interrupted prior to completion to highlight the initiation and propagation of the cracks. The profiles of this sample can be seen in Figure 4.18. Figure 4.18a shows that the cracks initiated parallel to the loading force, as well as on the surface where one would expect to find the shear bands. One of these cracks is then expected to propagate through the sample and result in fracture. In this case, it was the crack which initiated parallel to the loading force. Figure 4.18b shows that the crack is not perfectly linear through the sample.

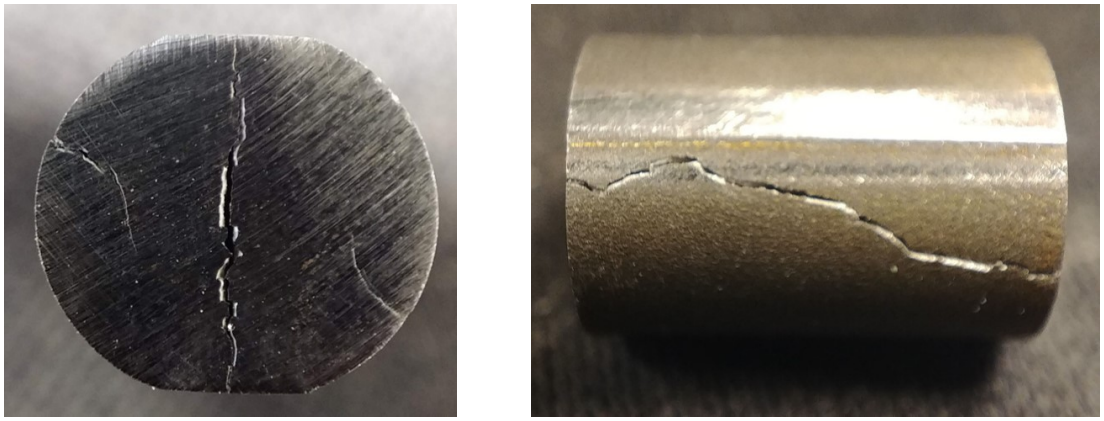

(a) Fracture through the side press sample (b) Fracture along the side press sample

Figure 4.18: Photos of interrupted side press test

Figures 4.19 and 4.20 show the fracture surface of a D2 side press compression sample. The middle of the sample appears more dull and is marked by a △ symbol on Figure 4.19. It is shown in Figure 4.20b, where the fracture of large carbides is dominant, with small amounts of ductile fracture surrounding smaller carbides. The fracture of the large carbides is consistent with cleavage fracture, where multiple steps and planes are apparent. The fracture along the edge of the sample appears shinier and is marked by a ◯ symbol symbol on Figure 4.19. Figure 4.20a shows sheared dimples, as well as a small cracked carbide in the bottom right corner, and other small distributed carbides throughout.

Figure 4.19: Photo of D2 side press fracture surface

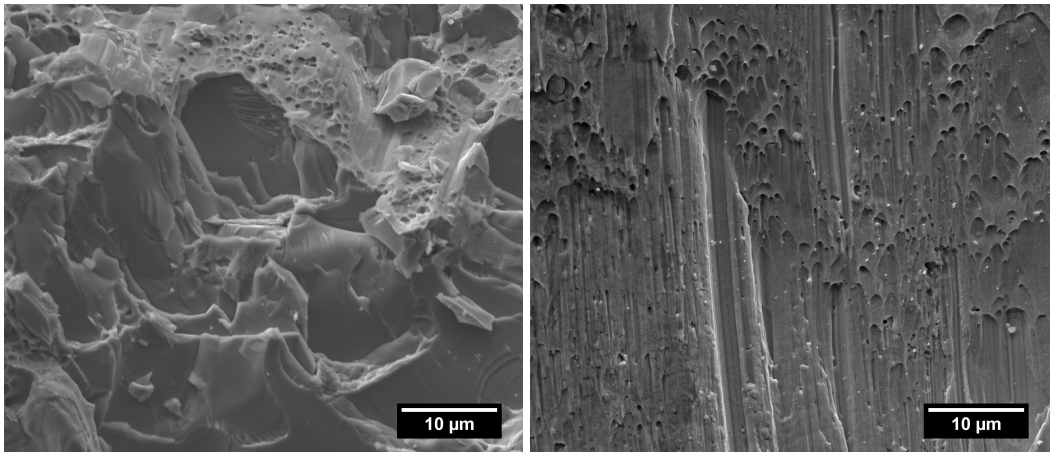

(a) X1000 SE (△) (b) X1000 SE (◯)

Figure 4.20: SEM Images of D2 side press fracture surface

Figures 4.21 and 4.22 show the fracture surface of a Carmo side press compression sample. Figures 4.22a and 4.22b are images taken from a raised area, denoted by a ◯ symbol in Figure 4.21. Figure 4.22a does not show much definition in the fracture surface; Figure 4.22b shows sheared dimples, similar to those present along the edge of the D2 side press fracture surface shown in Figure 4.20a. The area along where a △ symbol is shown on Figure 4.21 is more dull than the rest of the fracture surface. It appears to be a ridge and is somewhat perpendicular to the plane shown in the image in Figure 4.22a, and the region in Figure 4.21 denoted by a ◯ symbol. Figure 4.22c shows that the fracture mode here appears to be quasi-cleavage fracture. Figure 4.22d shows the fracture surface of the area denoted by a ◊ symbol in Figure 4.21. The fracture surface also appears to be quasi-cleavage, though with more planes and variation in depth, as well as some small amount of ductility surrounding small carbides.

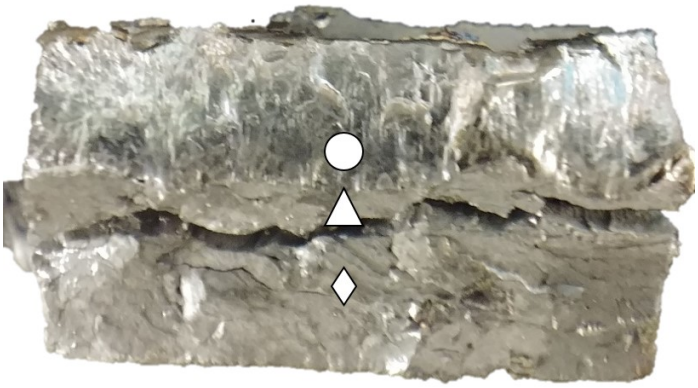

Figure 4.21: Photo of Carmo side press fracture surface

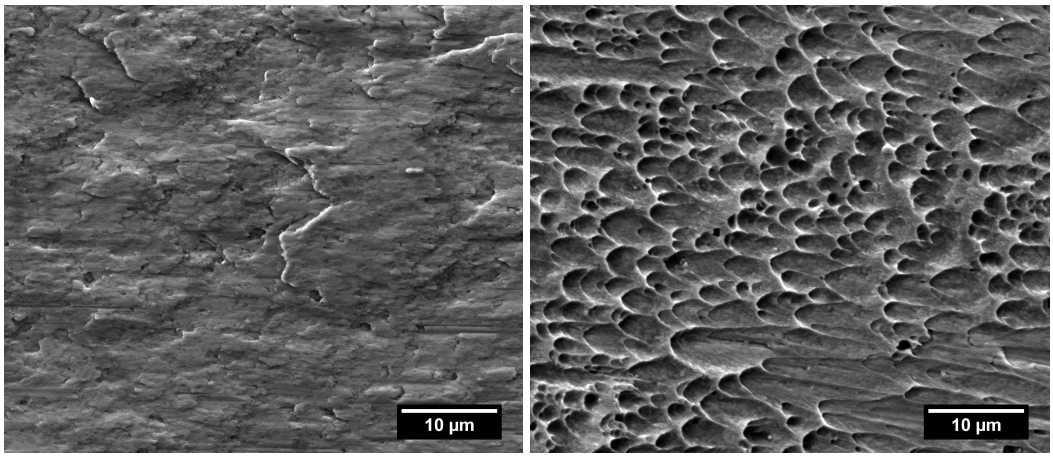

(a) SE - X1000 (◯) (b) SE - X1000 (◯)

(c) SE - X1000 (△) (d) SE - X1000(◊)

Figure 4.22: SEM Images of Carmo side press fracture surface

Figures 4.23 and 4.24 show the fracture surface of a Caldie side press compression sample. The fracture surface in the corner is marked by a ◯ symbol in Figure 4.23. Figure

4.24a shows that this area appears to be a mixture of quasi-cleavage and ductile fracture around very small particles. Figure 4.24b shows the fracture surface at the edge of the sample, marked by a △ symbol in Figure 4.23. Clear curved cleavage steps can be seen in this area, both macroscopically, and microscopically. The fracture surface shown in Figure 4.24c is locarted in the area marked by a ◊ symbol. The fracture surface here appears very similar to that shown in Carmo in Figure 4.22c and further highlights the quasi-cleavage fracture which occurs in Caldie.

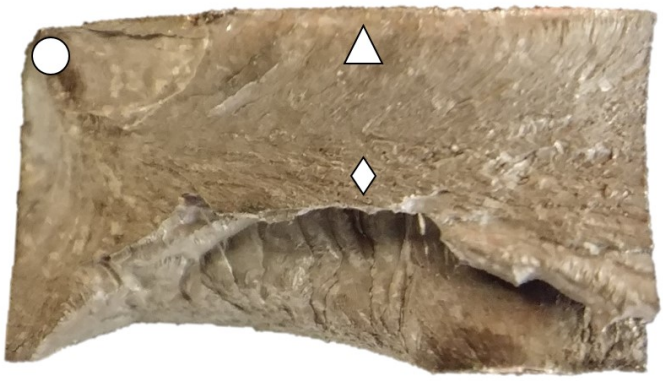

Figure 4.23: Photo of Caldie side press fracture surface

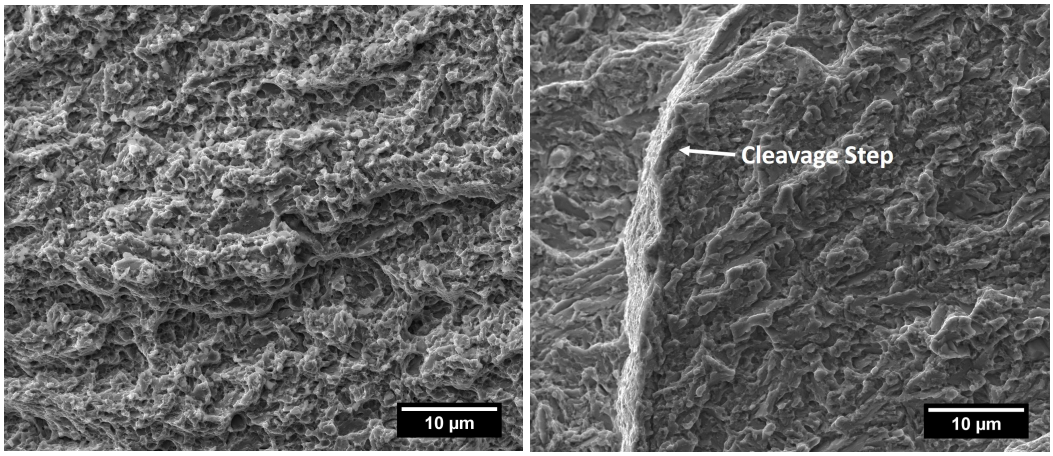

(a) X1000 SE (◯) (b) X1000 SE (△)

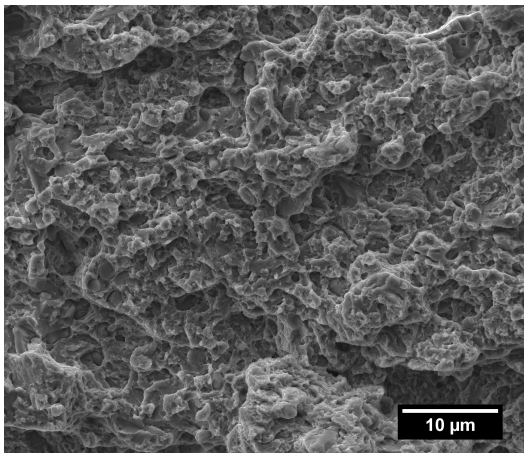

(c) X1000 SE (◊)

Figure 4.24: SEM Images of Caldie side press fracture surface

4.6 Summary of Results

The following table gives a summary of the key mechanical test results. Stress/strain curve characteristics are compared in the first two rows, followed by fracture characteristics.

Table 4.3: Summary of mechanical testing results

	D2	**Carmo**	**Caldie**
Tension Stress/Strain	-No plastic deformation -Lowest fracture stress/strain	-Inconsistent -Fractured before or just after yield point	-Plastic deformation -Highest fracture stress/strain
Compression Stress/Strain	-Lowest fracture stress/strain	-Inconsistent -Highest fracture stress/strain	-Higher fracture stress
Fracture Characteristics	-Carbide cleavage fracture + dimples -Large primary carbides dominate fracture mechanism -Stress triaxiality has no visible effect on fracture morphology	-Quasi-cleavage fracture -Impurities -Stress triaxiality	-Quasi-cleavage fracture -Very small carbides influence fracture -Very homogenous fracture surfaces

A significant outcome of this study is the data that can be used as input into a material model for finite element simulation of the damage accumulation in the trim die. The following tables provide a useful correlation between the stress triaxiality factor and the fracture stress and strain data that was previously presented in Tables 4.1 and 4.2.

Table 4.4: D2 Fracture Data in terms of stress triaxiality

Test	**Triaxiality**	**Fracture Strain**	**Fracture Stress**
Compression	-0.33	12.61 $\pm$ 1.60 %	3425 $\pm$ 90 MPa
Compression Shear	-0.2		
Tension	0.33	0.43 $\pm$ 0.03 %	816 $\pm$ 65 MPa

Table 4.5: Carmo Fracture Data in terms of stress triaxiality

Test	**Triaxiality**	**Fracture Strain**	**Fracture Stress**
Compression	-0.33	19.83 $\pm$ 0.51 %	4128 $\pm$ 156 MPa
Compression Shear	-0.2		
Tension	0.33	0.76 $\pm$ 0.19 %	1267 $\pm$ 192 MPa

Table 4.6: Caldie Fracture Data in terms of stress triaxiality

Test	**Triaxiality**	**Fracture Strain**	**Fracture Stress**
Compression	-0.33	12.98 $\pm$ 0.51 %	3912 $\pm$ 259 MPa
Compression Shear	-0.2		
Tension	0.33	1.64 $\pm$ 0.36 %	2219 $\pm$ 196 MPa

4.7 Trim Die Wear Analysis

Two sets of trim die inserts were analyzed after 40,000 trimming cycles. The resultant volume loss along the trim edge is recorded in Tables 4.7 and 4.8. The volumetric wear loss is also shown as a bar chart in Figure 4.25 to better visualize these data.

Table 4.7: Volumetric loss and wear rate for D2 steel dies after 40,000 trim cycles

Tool/plane	**D2 upper sliding plane**	**D2 lower sliding plane**	**D2 upper impact plane**	**D2 lower impact plane**
Volumetric loss (m^3)	3.78E-11	5.35E-11	3.05E-11	5.06E-11
Wear rate (m^3/cycle)	9.45E-16	1.33E-15	7.60E-16	4.38E-16

Table 4.8: Volumetric loss and wear rate for Carmo and Caldie dies after 40,000 trim cycles

Tool/plane	**Carmo upper sliding plane**	**Caldie lower sliding plane**	**Carmo upper impact plane**	**Caldie lower impact plane**
Volumetric loss (m^3)	4.93E-12	4.43E-11	1.19E-11	1.75E-11
Wear rate (m^3/cycle)	1.23E-16	1.10E-15	2.90E-16	4.38E-16

It is of note that the volume loss for the D2 samples is consistently higher across all samples. D2 had large amounts of chipping which caused high volume loss with significant variation across the areas measured; this is very evident in Figure 4.25. The volume loss in Caldie is principally attributed to the peeling off of the TiCN coating, as opposed to material loss of the substrate or chipping.

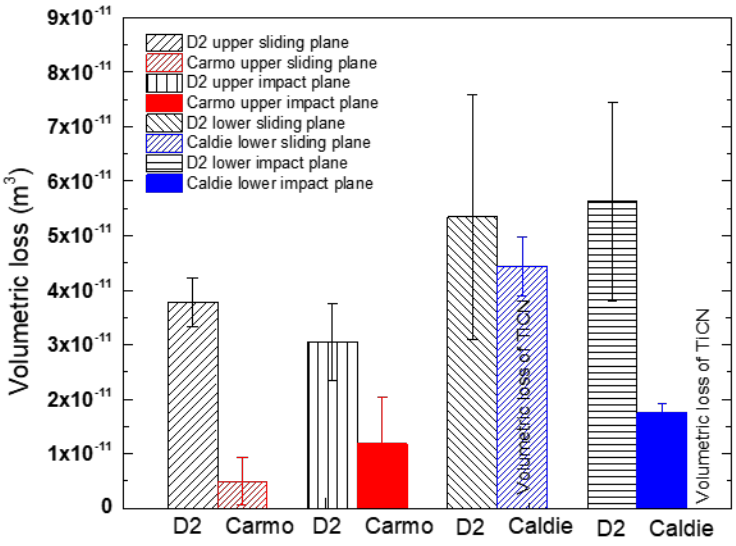

Figure 4.25: Volumetric loss after 40,000 trimming cycles

4.7.1 Surface Topography of the Planes Adjacent to the Trim Edge

Three-dimensional optical profilometry images of the impact and sliding planes adjacent to the trim edge after 40,000 trimming cycles are shown in Figure 4.27. In each image, the trim die edge is located at the bottom of the image. The horizontal lines that can be seen along the top of many of the images are residual grinding marks, and are areas which have not been subjected to friction or wear in the trimming process. A representative image showing the trim edge location and the dimensions of the area that was scanned is shown in Figure 4.26.

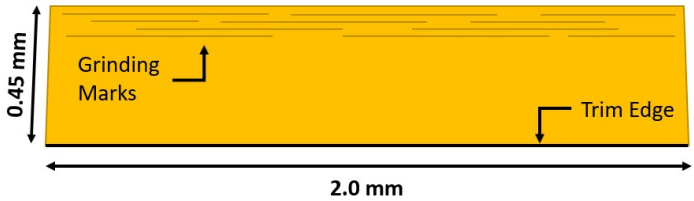

Figure 4.26: Image depicting representative profile of trim edge

The significant difference in material loss between the D2 and Carmo upper sliding planes shown by the bar chart in Figure 4.25 is visually depicted in Figures 4.27a and b. In both materials, much of the material at the trim edge is removed or displaced due to abrasive wear. This is visually represented by the lighter areas closer to the trim edge and the darker red areas farther away, where at least some of the material was removed by the trimming operation.

The greater volume loss in the Carmo upper impact plane when compared to that of the upper sliding plane can be explained by the chipping that occurred sporadically across the trim edge. The trim edge of both the Carmo and D2 inserts show evidence of material removal along the edge which resulted in an increase of volume loss when compared to purely abrasive wear.

The sliding planes on the lower trim dies show a significant amount of wear, as expressed in the bar chart in Figure 4.25. The lower sliding plane for D2 is shown in Figure 4.27e. There is very obvious chipping at the trim edge (these areas are shown in blue). The lighter areas are where the die material was removed due to abrasive wear. In Caldie, the material loss has been shown to be due to the removal of the coating which protects the substrate [4]. This can be seen visually in Figure 2.13b and c, where the TiCN coating has been removed, but the Caldie beneath is cracked, but whole.

The material loss in the D2 lower sliding plane is consistent with that of the D2 lower impact plane. The material loss due to chipping on the trim edge that can be seen in blue in the D2 lower sliding plane in Figure 4.27e can also be seen in Figure 4.27g. In comparison, there is much less material loss in the Caldie lower impact plane as shown in Figure 4.27h. The lighter spots are not due to abrasive wear, but rather inconsistent coating application, as this can be seen on the as received trim die.

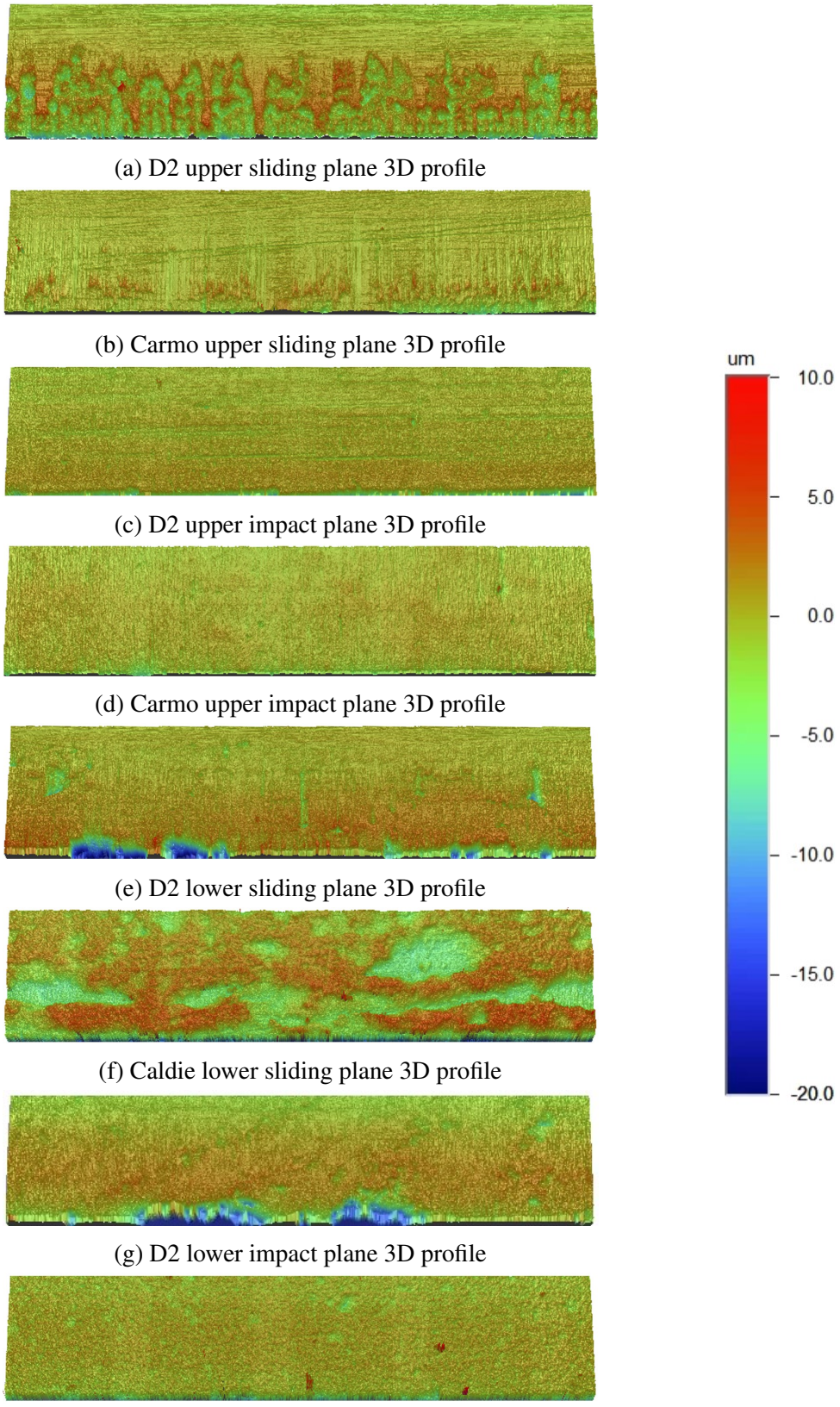

(a) D2 upper sliding plane 3D profile

(b) Carmo upper sliding plane 3D profile

(c) D2 upper impact plane 3D profile

(d) Carmo upper impact plane 3D profile

(e) D2 lower sliding plane 3D profile

(f) Caldie lower sliding plane 3D profile

(g) D2 lower impact plane 3D profile

(h) Caldie lower impact plane 3D profile

Figure 4.27: 3D Profiles of trim die sliding and impact surfaces

Chapter 5

Discussion

5.1 Microstructure

A variety of alloy contents, processing, and heat treatments have been used to produce tool steels with a mix of microstructures. Each has its own benefits. D2 has been produced as an affordable tool steel which does not require special processing or additional tempering operations. The high chromium content results in large, banding, M_3C_7 carbides. These carbides are necessary to reach the initial wear resistance required as they are harder than the surrounding martensite matrix. This relationship is generally expressed by Equation 5.1 [21], where, W, the worn volume, is inversely related to p_m, the flow pressure, or softness of the material. In tool steels, there are other considerations beyond hardness. The carbide size and distribution play a significant role in wear resistance. Additionally, the response to stresses in different stress triaxialities shows that the large carbides play a role in decreasing the material's resistance to fracture. The effect of this banding can be seen to be a primary fracture mechanism in Figure 4.7. It is believed that this fracture surface was created when the sample impacted the platen. It is possible that future testing will reveal more effects of the banding in high strain rate testing.

$$W = KsP/p_m \tag{5.1}$$

Higher chromium and vanadium content typically result in a higher strength. D2, with 0.5 - 1.10 wt.% V and 11 - 13 wt.% Cr had a tensile and compressive strength below that of Caldie with 0.5 wt.% V and 5.0 wt.% Cr. The size and distribution of carbides appears to have a larger effect on the behaviour of the tool steel than the alloy content.

Carmo uses a traditional casting technique and two tempering cycles. The lower chromium and carbon contents result in more evenly distributed, smaller carbides. Caldie uses more expensive techniques. After being traditionally cast, ESR is then conducted to produce a cleaner, more homogeneous, microstructure. Caldie is also triple-tempered at a higher temperature than either D2 or Carmo. The high temperature and multiple tempering cycles transform the remaining retained austenite to martensite, and result in the $<2\%$ retained austenite in Caldie. The secondary carbides in Caldie appear to be less numerous than those in Carmo; however, they are supplemented by small "tempering carbides" which appear in Figure 4.2. The higher Mo and V content in Caldie contribute to the formation of nano sized MC and M_2C carbides [5]. These factors likely contribute to higher costs in producing Caldie, but have a clear effect on the consistency in both flow curves, and in fracture surfaces. This is most apparent when comparing the fracture surfaces across triaxialities, or when comparing the tool steel behaviours in tension. The Caldie samples performed to a significantly higher tensile stress and strain, as shown in Figure 4.11.

The amount of retained austenite in the material does not appear to have as much of an effect as would be expected when compared to the carbide size and distribution. Carmo is expected to have approximately 10% retained austenite given its heat treatment. This is much higher than the $<2\%$ retained austenite found in Caldie, due to the triple tempering performed at high temperatures of 540°C, which has been shown to transform the retained austenite to martensite. However, D2 is expected to have approximately 15 to 22% retained austenite given its heat treatment [45]. The literature points to retained austenite as a way of absorbing energy and resisting crack propagation [24]. D2 has the highest % retained austenite, which is in contrast to the trimming results, which showed that D2 had the highest rate of chipping. It would also be expected that D2 have an increased strain at fracture when compared to Caldie or Carmo which both had a lower % retained austenite. This is not the case in tension or compression. It is possible that in the multiple tempering cycles,

the Carmo and Caldie were able to temper more of the martensite, which would lead to a higher ductility.

The microstructure analysis of the three tool steels is of interest as they quantify the carbide distribution. Unfortunately, it is quite difficult to capture the distribution of D2 when compared to Carmo and Caldie. This is due to the magnitude of difference in carbide size. D2 clearly shows large bands of carbides as in Figure 4.1a. SEM of Carmo and Caldie at this scale does not capture the carbides at all. They are too small. Carbides in D2 can be in excess of 100μm long, while all of the carbides in Carmo and Caldie are approximately 1μm or less in length. Therefore, this analysis may be skewed in favour of smaller carbides in D2. Particularly those which could fit within the area used in the analysis. The large carbides in D2 also result in a large variation in size of carbide. Figure 4.1b and in turn, Figure 4.4 show D2 carbides which are less than a micron in length. This variation is not seen in Carmo or Caldie. Caldie has a larger variation in aspect ratio, and the carbides seem to form along what appear to be grain boundaries. This is offset by the numerous nano-sized particles present in the Caldie microstructure which form within the matrix, as shown in Figure 4.1f. Carmo appears to have very consistently shaped carbides that are well distributed within the matrix.

5.2 Mechanical Properties

The difference in the mechanical behaviour between tension and compression highlight the importance of this work.

5.2.1 Compression Testing

For the compression testing, the materials exhibited distinct behaviours as shown by the flow curve in Figure 4.6. The elastic moduli appear very similar. The stress and strains at fracture, as well as the flow curves themselves are very different. D2 is the baseline, with the lowest fracture strength and fracture strain. The curves for Caldie and Carmo exist above the curves for D2. Caldie has a higher strength than D2, but only a marginally higher fracture strain on average. Carmo has a higher fracture stress and strain when compared

to both Caldie and D2. Carmo exceeds D2 by almost 10% strain before failure. This may be due to the much smaller carbides in Carmo which are distributed within the matrix. This has been shown to increase the fracture toughness by forcing the crack through the relatively ductile matrix [17]. The large carbides in D2 are likely the site of crack initiation and propagation, leading to a large portion of the fracture surface to be cleavage fracture, as shown in Figure 4.8a. Another possible cause of this phenomena is the additional tempering step in Carmo when compared to D2. Additional tempering can lead to increased ductility as more of the as-quenched martensite is transformed to tempered martensite. The variation in the results for Carmo in compression is likely due to the impurities shown in Carmo, as seen in Section 4.3.1. Caldie exceeded both D2 and Carmo in yield strength, by 500MPa on average. This is a key property given for tool steels and is the only property available in data sheets which advertises the material's strength.

5.2.2 Tensile Testing

In tension, an increase in strength and ductility occur simultaneously from D2 to Carmo to Caldie. The baseline D2 has the lowest fracture stress and strain, fracturing in the elastic portion. Carmo has a similar behaviour to D2. The stress and strain at fracture are higher for Carmo; however, the material still fractures in, or just beyond, the elastic portion of the deformation. It is possible that Carmo would reach higher stresses and strains if the processing were improved. The data in compression suggests that it is capable of much higher strains when compared to D2 and Caldie. It is likely that the impurities act as fracture initiation points, similarly to how the large carbides act to initiate fracture in D2. This would go to link the behaviours and explain why they broke prior to deforming plastically. In contrast, Caldie exhibited plastic deformation with significantly higher fracture stresses and strains. This is different from the behaviour of Caldie in compression. Caldie had extensive processing, including ESR and triple tempering to ensure a clean and strong final product. This is reflected in the higher ductility compared to Carmo and D2 in tension.

Overall, there is more consistency in the tensile results when compared to compression. Each of the three tool steels followed the same tensile curve for the tests without

significant deviation. This could be due to a higher sensitivity to impurities in tension. The samples in compression follows a shear band which can accommodate more strain. This allows for the fractures to close and for the material to continue deforming.

5.3 Fractography

Due to the brittle nature of the material, the microstructure has a large effect on how the material fails. The effect of the distribution, type and volume fraction of carbides has been documented in other pieces of literature [17, 28, 16].

In comparison, Caldie shows a very uniform fracture in tension and compression. The fracture surface does not show the same evidence of cleavage fracture through carbides. The dominant mode of fracture appears to be quasi-cleavage fracture. Despite this being a usual clear sign of hydrogen embrittlement, this is not the case here. Past research shows that tool steels are capable of quasi-cleavage fracture when the matrix is made up of plate martensite [17]. According to the paper that saw this phenomenon occur, steels with a matrix containing more than 0.4 wt. % C are suggested to result in plate martensite. According to Bhadeshia and Honeycombe [30], lath martensite forms in steels containing up to 0.5 wt. % C. Plate martensite is formed in higher carbon steels. Lath and plate martensite form concurrently in steels containing between 0.5 and 1.0 wt. % C. Given this information, it is likely that all three materials contain plate martensite. As Carmo and Caldie have very small carbides which primarily form within the matrix, as opposed to along grain or cell boundaries, the fracture is likely moving through the relatively ductile matrix. The quasi-cleavage fracture observed can validate this prediction, as it is congruent with fracture of the martensite plates. This is ideal, as it requires more energy to be expended to fracture, as reinforced by the mechanical test results in Sections 4.2 and 4.3. However, D2 would contain a larger fraction of plate martensite in comparison to Carmo and Caldie. The fracture of the small portion of the matrix in D2 was ductile, not quasi-cleavage. This suggests that there are more factors at play in producing quasi-cleavage fracture than simply the type of martensite. Further microstructural characterization through SEM and transmission electron microscopy (TEM) analysis are advised for better understanding of such phenomena.

It is theorized that the large carbides in D2 dominated the fracture, and the more uniform dispersion of micro- and nano-sized particles in Carmo and Caldie led to large scale dimples to form with localized quasi-cleavage fracture through the plate martensite. Something that would not be possible in D2.

Large M_7C_3 carbides tend to form along grain boundaries. The initiation of cracks in M_7C_3 carbides has been shown in the literature to result in a lower fracture toughness when compared to a tool steel which exhibits the same quasi-cleavage fracture seen in the tensile and compression fracture surfaces for Caldie and Carmo [17]. It can be seen in Figure 4.12b that the fracture of these carbides dominates the fracture surface, and defines the dominant mode of fracture for the D2 steel. This is true across the stress triaxialities; the fracture surface in compression appears to be very similar to that in tension.

In terms of trimming, this can be shown in the rate of chipping. The fracture of large carbides begins early in the process and likely leads to a higher rate of chipping. This can be supported by the higher rate of chipping in D2 when compared to Carmo and Caldie.

Carmo exhibits occasional chipping in the trimming trials and lower strength in tension compared to Caldie. This can be explained by the lack of cleanliness when compared to Caldie. The fracture surfaces for the mechanical tests performed on Carmo showed evidence of MnS inclusions, as well as V and Cr concentrations which appeared to be either plate or needle-like in morphology. These inclusions and deviations from homogeneity result in initiation and propagation of fracture. The overall tensile fracture surface shown in Figure 4.12c exhibits bulk ductile failure in the form of a ductile lip around the perimeter of the sample. However, this is not reflected in the percent elongation in tension, which shows less plastic deformation than Caldie. Caldie does not exhibit the same ductile lips. It is more than likely that this is due to the weakening brought on by the impurities. Intergranular fracture in Carmo in tension also suggests weakness of the material due to unclean processing. No intergranular fracture was seen on any of the D2 or Caldie fracture surfaces. This information supports that the processing used on Carmo resulted in a less than ideal material.

5.3.1 Shear Compression

The Caldie shear compression fracture surface lacks definition. Its appearance resembles the Carmo compression or side press fracture. The flat areas are those that appear to have gone through galling. The bumpy areas are likely a combination of ductile and brittle fracture, similar to the quasi-cleavage fracture seen in the other samples. However, in this case the surface appears to have a direction, which is not surprising given it is shear fracture. The appearance of the fracture in shear compression shown in Figure 2.13a is very similar to the appearance of the sliding plane near the trim edge of the Carmo trim die, as shown in Figure 4.16. Both have direction and appear to have movement of the material in the ”sliding direction.”

The fracture surfaces found on the three materials are very similar, transcending the stress triaxiality. Cleavage planes, quasi-cleavage fracture, and small scale ductility are present in all materials observed.

5.4 Trim Die Wear

As mentioned, there is a difference in how the three materials performed in the trimming experiments. The D2 was notable in the large amount of chipping present across the surface. This is consistent with the assertion that the D2 would be more likely to crack and fracture, thus leading to a greater loss of material overall. The Carmo experienced much less material loss compared to the D2 and the Caldie. There were intermittent cracks due to high impact loads. The presence of impurities likely provided sites for crack initiation. The cracks in Carmo were not nearly as frequent as the D2 chips. The Caldie exhibited a high material loss compared to Carmo; however, this is due to the premature removal of the protective TiCN coating from the surface of the lower insert. The die material itself was mostly undamaged. A possible source of a chip site can be seen in Figure 2.13c, as cracks begin to form parallel to the trim edge. This is in a better condition than the other two trim die materials, as the only material loss appears to be in the removal of the coating and not the die steel itself. This is in contrast to the literature which showed minimal change in the trim edge geometry in a coated D2 sample.

The literature, as summarised in Section 2.7, calls out two methods of increasing the effectiveness of coatings on tool steels. The first is in the method of coating, between CVD, PVD, and TD. The TD coating appears to have the greatest adhesion; however, it might be difficult to achieve with Caldie, given its extensive heat treatment requirements. A PVD coating is the next most adhesive coating. The other method of increasing the coating effectiveness is in increasing the hardness of the substrate. The Caldie used in this study had a hardness of 62 ± 1 HRC, which is high for a tool steel. Nevertheless the peeling away of the TiCN coating after only 40,000 trimming cycles was unexpected. The adhesion of the coating does not appear to be uniform on the die surface, which may have contributed to the decohesion of the coating.

In past trimming trials performed at Oakland University, there was a higher rate of chipping observed on the sliding and impact planes on the lower die when compared to the upper die. The results also showed higher surface roughness on the sliding plane. There is not as clear of a comparison between sliding and impact planes in this analysis; however, it can be seen in Tables 4.7 and 4.8 and Figure 4.25 that this higher rate of volume loss occurs in the lower die.

It is important to consider the fracture surfaces of the mechanical test samples in relation to how damage is accrued on the die surface. Compression, shear, and tensile loads are applied to the trim edge throughout each trimming cycle and contribute to its failure. In past work, it was determined that the alloying elements, and thus the resultant alloyed carbides and microstructure, can be linked to the fracture toughness of the tool steel [12, 17]. This has also been shown in the current work. The large M_7C_3 carbides in D2 contribute greatly to its lower fracture strains in both tension and compression and have been shown to be the location for large cleavage planes to develop. This translated to significantly more chipping present in the D2 tool edge when compared to the other two materials. This can be extended to other parts of the microstructure as well, as the type of martensite, as well as the dispersion of nano-carbides within the martensite matrix have been shown to have an effect on the type of fracture in the tool steel.

Chapter 6

Conclusions

The following conclusions can be drawn from the work that was carried out.

Structure

- The structure of the carbides can be well documented using number of carbides, area fraction, length, and aspect ratio.
- Carmo and Caldie had smaller, more evenly dispersed carbides which are shown to improve fracture toughness and wear resistance.
- The homogeneity of the microstructure can be related to the same homogeneity in the fracture surfaces. This is especially clear when comparing D2 and Caldie
- The material's microstructure becomes especially important when looking at such a brittle material where any in-homogeneity can lead to the initiation or propagation of a crack.

Processing

- Processing had the largest effect on Carmo. The impurities and voids which appeared due to inconsistent processing limited the capabilities of the material. This lead to not only the appearance of impurities in the sample, but also of intergranular fracture in tension.

- Tempering of the tool steels allowed for greater ductility in the martensite. Cup and cone fracture appeared in D2, and quasi-cleavage fracture occurred in Carmo and Caldie. This tempering is directly correlated to the improved fracture toughness of the tool steel.
- The tempering cycles applied to Caldie allowed for the production of nano-carbides which appear to have an influence on the fracture behaviour, and mechanical properties as a whole

Performance

- A new method was developed to determine the volume of material lost across the trim edge after a number of trimming cycles have been performed. This method is effective at documenting the material lost due to the TiCN coating, or from chipping and was able to quantify the differences in wear between the tool steels.
- By quantifying the material loss across the surface, it is possible to directly confirm the wear damage that will be predicted by future FEA analysis.

Properties

- Mechanical testing of tool steels is often not used to its full potential. Usually, the only mechanical properties given are the yield strength and Young's modulus. This is insufficient to understand the material and how it will behave.
- Each of the mechanical tests conducted have a benefit in the chatacterization process. Tensile testing in particular reveals the weakness of the structure and provides insight into where and how the material may fail. Whereas the side press test revealed many fracture behaviours on a single sample. Compression and compression shear testing represent more traditional approaches to characterizing tool steels, and are representative of the stresses present in the trimming process.
- The flow curves and the mechanical properties which can be derived from mechanical testing offer invaluable guidance as to the effect of the material alloys and processing.

- By comparing the fracture surfaces, it is possible to predict how these materials will behave in more complex operations, such as trimming.
- Capturing the elastic, plastic, and fracture behaviour is very important as the tool steels being produced become more complex.
- Due to the brittle nature of the materials, they are sensitive to changes in microstructure or to impurities which will affect the mechanical properties and ultimately the performance of the material.

6.1 Future Work

Though not discussed in this text, the banding of carbides shown in D2 may lead to anisotropy in the material behaviour and mechanical properties. Future studies should investigate the magnitude of this effect on the material's properties, such as tensile strength. Further work should also focus on high strain rate testing to determine if the banding shown in the fracture surface of the specimen tested in compression appears in samples tested with a more convensional aparatus such as a Split-Hopkinson pressure bar. Nano-particles and their effect on fracture were also beyond the scope of what is discussed within this work. They appear to have a significant effect on the fracture and wear behaviour of the tool steel, given its secondary hardening effect and the complexity it brings beyond a two-phase system with larger carbides within a tempered martensite matrix.

This work, in part, was intended as use for developing inputs to a material model used in simulating the damage accumulation and wear of trim dies. It is expected that this work will fuel more research in this area, and be further optimised for use in industrial applications. Ideally, this work will be used to reduce tool costs through improved CAE analysis.

6.1.1 Challenges in Testing

It is critical that when performing tests on tool steel in the future that certain challenges be kept in mind. The tool steel is of equal hardness to the steel used in the platens and the

grips of the MTS universal testing machine. This resulted in many failed tests prior to obtaining the results shown in this study. For example, in the initial compression tests, there was unexpected deformation of the platens which resulted in broken platens. This required the platens to be made twice as thick.

Additional issues arose when performing DIC analysis. The test specimens used were sub-sized, as the high strength of the material limited the cross sectional area. To obtain an adequate strain reading, the speckle pattern applied had to have a high density of small black paint specks in an even distribution across a very small area. This requires experimentation of the spray paint nozzle type. An image of the nozzle used for this study can be seen in Appendix A.

Bibliography

[1] Transportation Research Board and National Research Council, *Effectiveness and Impact of Corporate Average Fuel Economy (CAFE) Standards*. Washington, DC: The National Academies Press, 2002. [Online]. Available: https://www.nap.edu/catalog/10172/effectiveness-and-impact-of-corporate-average-fuel-economy-cafe-standards

[2] M. P. Pereira, W. Yan, and B. F. Rolfe, "Wear at the die radius in sheet metal stamping," *Wear*, vol. 274-275, pp. 355–367, 2012.

[3] S. F. Golovashchenko, "A study on trimming of aluminum autobody sheet and development of a new robust process eliminating burrs and slivers," *International Journal of Mechanical Sciences*, vol. 48, no. 12, pp. 1384 – 1400, 2006.

[4] Z. Cui, S. Bhattacharya, D. Green, and A. Alpas, "Mechanisms of die wear and wear-induced damage at the trimmed edge of high strength steel sheets," *Wear*, vol. 426-427, pp. 1635 – 1645, 2019, 22nd International Conference on Wear of Materials.

[5] M. A. Rehan, "Microstructure and mechanical properties of a 5 wt.% Cr cold work tool steel - Influence of heat treatment procedure," no. 18, 2017.

[6] J. Cross, R. Opila, I. Boyd, and E. Kaufmann, "Materials characterization and the evolution of materials," *MRS Bulletin*, vol. 40, pp. 1019–1034, 12 2015.

[7] A. M. Bayer and L. R. Walton, "Wrought Tool Steels," in *Properties and Selection: Irons, Steels, and High-Performance Alloys*. ASM International, 01 1990.

[8] G. Roberts, R. Kennedy, and G. Krauss, *Tool Steels, 5th Edition*, ser. EngineeringPro collection. ASM International, 1998.

[9] B. Mishra, “Steelmaking Practices and Their Influence on Properties,” in *Metals Handbook Desk Edition*. ASM International, 12 1998.

[10] G. F. Vander Voort, “Martensitic Structures,” in *Metallography and Microstructures*. ASM International, 12 2004.

[11] R. A. Mesquita, R. S. Schneider, and C. S. Gonçalves, “Heat Treating of Cold-Work Tool Steels—Medium-Alloy Air-Hardening, High-Carbon High-Chromium and High-Vanadium-Powder Metallurgy Steels,” in *Heat Treating of Irons and Steels*. ASM International, 10 2014.

[12] K. C. Hwang, S. Lee, and H. C. Lee, “Effects of alloying elements on microstructure and fracture properties of cast high speed steel rolls: Part i: Microstructural analysis,” *Materials Science Engineering A*, vol. 254, no. 1-2, pp. 282–295, 1998.

[13] J. R. Davis, *Metals Handbook Desk Edition*. ASM International, 12 1998.

[14] D. C. Ko, S. G. Kim, and B. M. Kim, “Influence of microstructure on galling resistance of cold-work tool steels with different chemical compositions when sliding against ultra-high-strength steel sheets under dry condition,” *Wear*, vol. 338-339, pp. 362–371, 2015.

[15] R. L. Fullman, “Measurement of particle sizes in opaque bodies,” *The Journal of The Minerals, Metals & Materials Society*, vol. 5, no. 3, pp. 447–452, Mar 1953.

[16] B. Edelson and W. Baldwin, Jr, “The effect of second phases on the mechanical properties of alloys,” Tech. Rep., 1959.

[17] K. C. Hwang, S. Lee, and H. C. Lee, “Effects of alloying elements on microstructure and fracture properties of cast high speed steel rolls: Part ii. fracture behavior,” *Materials Science Engineering A*, vol. 254, no. 1-2, pp. 296–304, 1998.

[18] S. Bhattacharya, D. Green, R. Sohmshetty, and A. Alpas, “Wear of d2 tool steel dies during trimming dp980-type advanced high strength steel (ahss) for automotive parts,” *SAE Technical Paper*, 2017.

[19] Ö. N. Cora and M. Koç, "Experimental investigations on wear resistance characteristics of alternative die materials for stamping of advanced high-strength steels (AHSS)," *International Journal of Machine Tools and Manufacture*, vol. 49, no. 12-13, pp. 897–905, 2009.

[20] J. Schneckenleitner, R. Schneider, G. Rabler, C. Walch, E. Heinl, J. Mauser, and A. Hechtl, "Performance of different tool steels for the cutting of an cp1000 advanced high strength steel," *BHM Berg- und Hüttenmännische Monatshefte*, vol. 156, no. 3, pp. 105–111, Mar 2011.

[21] J. Archard and W. Hirst, "The Wear of Metals under Unlubricated Conditions," *Proceedings of the Royal Society of London. Series A, Mathematical and Physical Sciences*, vol. 236, no. 1206, pp. 397–410, 1956.

[22] G. F. Vander Voort, "Metallographic Techniques for Tool Steels," in *Metallography and Microstructures*. ASM International, 12 2004.

[23] A. Molinari, M. Pellizzari, S. Gialanella, G. Straffelini, and K. H. Stiasny, "Effect of deep cryogenic treatment on the mechanical properties of tool steels," *Journal of Materials Processing Technology*, vol. 118, no. 1-3, pp. 350–355, 2001.

[24] D. Das, A. K. Dutta, V. Toppo, and K. K. Ray, "Effect of deep cryogenic treatment on the carbide precipitation and tribological behavior of D2 steel," *Materials and Manufacturing Processes*, vol. 22, no. 4, pp. 474–480, 2007.

[25] R. Wu, W. Li, S. Zhou, Y. Zhong, L. Wang, and X. Jin, "Effect of retained austenite on the fracture toughness of quenching and partitioning (Q&P)-treated sheet steels," *Metallurgical and Materials Transactions A: Physical Metallurgy and Materials Science*, vol. 45, no. 4, pp. 1892–1902, 2014.

[26] Y. Lü, Q. Wang, X. Zeng, W. Ding, C. Zhai, and Y. Zhu, "Effects of rare earths on the microstructure, properties and fracture behavior of mg–al alloys," *Materials Science and Engineering: A*, vol. 278, no. 1, pp. 66 – 76, 2000.

[27] "Tool Steels: Atlas of Fractographs," in *Fractography*. ASM International, 01 1987.

[28] S. Lee, C. G. Lee, K.-S. Sohn, and B. I. Jung, "Correlation of microstructure and fracture toughness in three high-speed steel rolls," *Metallurgical and Materials Transactions A*, vol. 28, no. 1, pp. 123–134, Jan 1997.

[29] B. A. Miller, "Overload Failures," in *Failure Analysis and Prevention*. ASM International, 01 2002.

[30] H. Bhadeshia and R. Honeycombe, *Steels: Microstructure and Properties*. Butterworth-Heinemann, 2006.

[31] S. Fortuna, "Microstructural features of wear-resistant titanium nitride coatings deposited by different methods," *Thin Solid Films*, vol. 377-378, no. 1-2, pp. 512–517, 2000.

[32] R. Bunshah, "PVD and CVD Coatings," *ASM Handbook, Coatings, Friction, Lubrication, and Wear Technology*, vol. 18, pp. 840–849, 1992.

[33] I. Shigematsu, M. Nakamura, N. Saitou, and K. Shimojima, "Surface treatment of AZ91D magnesium alloy by aluminum diffusion coating," *Journal of Materials Science Letters*, vol. 19, no. 6, pp. 473–475, 2000.

[34] Ö. N. Cora, A. Ağcayaz, K. Namiki, H. Sofuoğlu, and M. Koç, "Die wear in stamping of advanced high strength steels - Investigations on the effects of substrate material and hard-coatings," *Tribology International*, vol. 52, pp. 50–60, 2012.

[35] Ö. N. Cora, K. Namiki, and M. Koç, "Wear performance assessment of alternative stamping die materials utilizing a novel test system," *Wear*, vol. 267, no. 5-8, pp. 1123–1129, 2009.

[36] Z. Cui, A. Rose, D. Green, J. Tjong, and A. Alpas, "Tribological performance of alternative die materials for trimming of advanced high strength steels," *Contributed Papers from Materials Science and Technology 2019*, 2019, paper presented at MST19, Portland, Oregon, USA. Warrendale, PA: Materials Science Technology.

[37] "ASTM E8/E8M-16a Standard Test Methods for Tension Testing of Metallic Materials," West Conshohocken, PA, 2016. [Online]. Available: https://doi-org/10.1520/E0008_E0008M-16A

[38] "ASTM E9-19 Standard Test Methods of Compression Testing of Metallic Materials at Room Temperature," West Conshohocken, PA, 2019. [Online]. Available: https://doi.org/10.1520/E0009-19

[39] A. Hassannejadasl, D. E. Green, W. J. Altenhof, C. Maris, and M. Mason, "Numerical modeling of multi-stage tube hydropiercing," *Materials Design*, vol. 46, pp. 235 – 246, 2013.

[40] "A681-08(2015) Standard Specification for Tool Steels Alloy," West Conshohocken, PA, 2015. [Online]. Available: https://www.astm.org/cgi-bin/resolver.cgi?A681-08(2015)

[41] "Carmo," pp. 1–7, 2005. [Online]. Available: https://www.uddeholm.com/files/PB_carmo-english.pdf

[42] "Uddeholm Caldie (R)," pp. 1–12, 2016. [Online]. Available: https://www.uddeholm.com/files/PB_caldie_english.pdf

[43] T. Rahmaan, A. Bardelcik, J. Imbert, C. Butcher, and M. Worswick, "Effect of strain rate on flow stress and anisotropy of dp600, trip780, and aa5182-o sheet metal alloys," *International Journal of Impact Engineering*, vol. 88, pp. 72 – 90, 2016.

[44] R. D. . G. A. Dorogoy, A., "Modification of the shear-compression specimen for large strain testing," *Exp Mech*, vol. 55, 2015.

[45] "Uddeholm Sverker (R) 21," pp. 1–12, 2016. [Online]. Available: https://www.uddeholm.com/files/PB_sverker_21_english.pdf

Appendices

Appendix A - Equipment

MTS Universal testing machines were used throughout the testing. Consistency in testing was obtained through use of only two of these machines, dependant on load requirements. The following are images of the equipment used to conduct the experiments, as outlined in Chapter 3.

Figure 6.1: MTS Universal Testing Machine with 600kN load cell with camera and light for compression testing

Figure 6.2: MTS Universal Testing Machine with 600kN load cell showing use of platens with compression sample

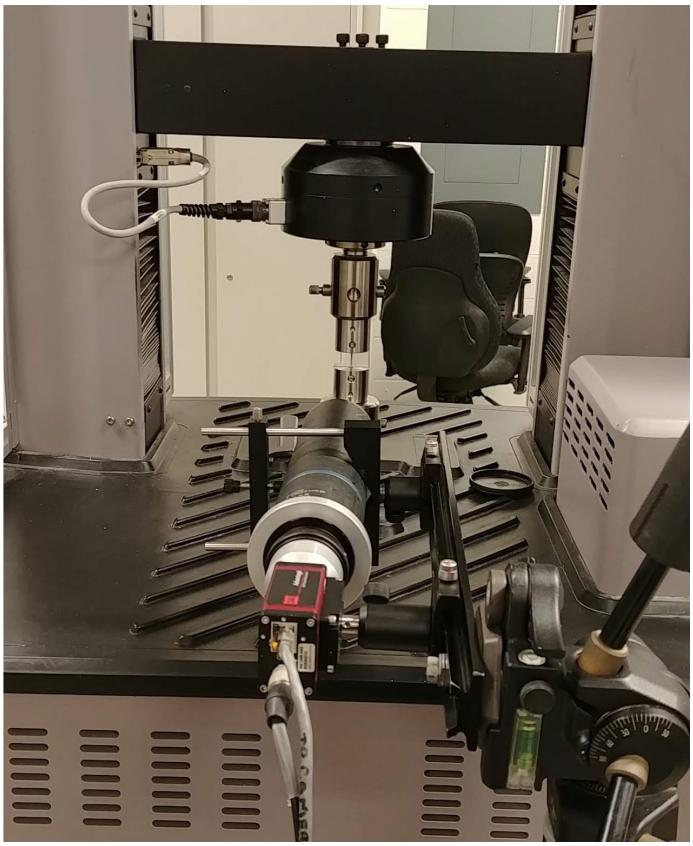

Figure 6.3: MTS Universal Testing Machine with 50kN load cell with camera and light for tensile testing, showing use of custom grips

Several spray nozzles were tested for their efficacy in producing a fine speckle pattern required for the test samples. This nozzle was found to be optimal for the application. The same nozzle was used to produce a speckle pattern on all samples. A sample of this pattern can be seen on a compression test sample in Figure 6.5.

Figure 6.4: Image of spray nozzle used to achieve speckle pattern shown in Figure 6.5

Appendix B - Test Samples

The following are images of samples used in testing. Figure 6.5 depicts a very difficult speckle pattern to achieve, which was used across all samples. Figure 6.6 gives some clarity to the sections taken for profilometry analysis which was ultimately used to quantify the volume lost in trimming.

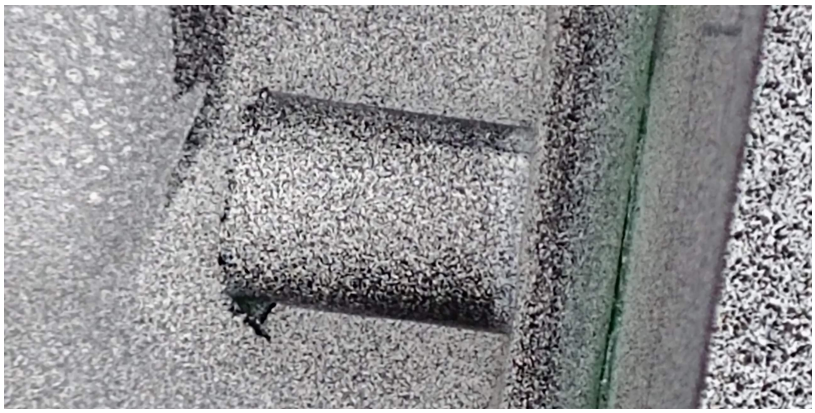

Figure 6.5: Image showing example speckle pattern applied to mechanical test samples

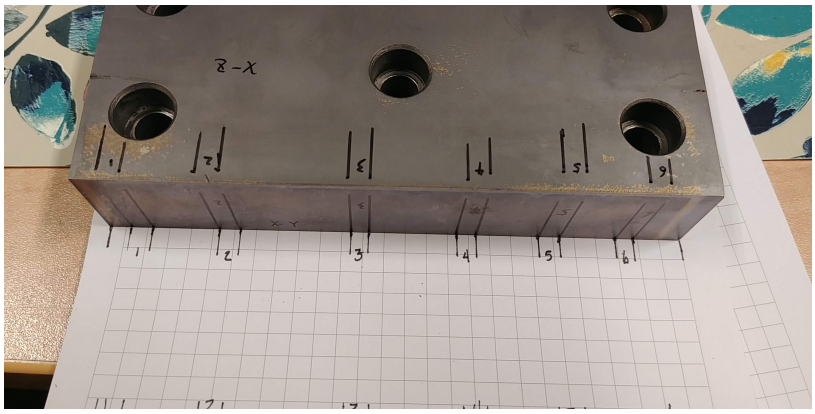

Figure 6.6: Image showing sections selected along trim die edge for profilometry analysis

Vita Auctoris

Alexandra Rose was born in 1994 in Windsor, Ontario. She completed her undergraduate degree in mechanical engineering at the University of Windsor in 2017, graduating with distinction and a specialization in materials. She completed her masters degree in materials engineering from the University of Windsor in 2020.